

# ODIN: The LAE Ly $\alpha$ Luminosity Function over Cosmic Time and Environmental Density

- GAUTAM NAGARAJ <sup>1</sup>, ROBIN CIARDULLO <sup>2,3</sup>, CARYL GRONWALL <sup>2,3</sup>, VANDANA RAMAKRISHNAN <sup>4</sup>,  
 KYOUNG-SOO LEE <sup>4</sup>, ERIC GAWISER <sup>5</sup>, NICOLE FIRESTONE <sup>5</sup>, GOVIND RAMGOPAL,<sup>5</sup> J. AGUILAR,<sup>6</sup> S. AHLEN,<sup>7</sup>  
 D. BIANCHI,<sup>8,9</sup> D. BROOKS,<sup>10</sup> F. J. CASTANDER,<sup>11,12</sup> T. CLAYBAUGH,<sup>6</sup> A. CUCEU,<sup>6</sup> A. DE LA MACORRA,<sup>13</sup> ARJUN DEY,<sup>14</sup>  
 BIPRATEEP DEY,<sup>15,16</sup> P. DOEL,<sup>10</sup> J. E. FORERO-ROMERO,<sup>17,18</sup> E. GAZTAÑAGA,<sup>11,19,12</sup> S. GONTCHO A GONTCHO,<sup>6,20</sup>  
 G. GUTIERREZ,<sup>21</sup> H. K. HERRERA-ALCANTAR,<sup>22,23</sup> K. HONSCHEID,<sup>24,25,26</sup> M. ISHAK,<sup>27</sup> R. KEHOE,<sup>28</sup> D. KIRKBY,<sup>29</sup>  
 T. KISNER,<sup>6</sup> A. KREMIN,<sup>6</sup> M. LANDRIAU,<sup>6</sup> L. LE GUILLOU,<sup>30</sup> M. E. LEVI,<sup>6</sup> C. MAGNEVILLE,<sup>23</sup> M. MANERA,<sup>31,32</sup>  
 P. MARTINI,<sup>24,33,26</sup> A. MEISNER,<sup>14</sup> R. MIQUEL,<sup>34,32</sup> J. MOUSTAKAS,<sup>35</sup> N. PALANQUE-DELABROUILLE,<sup>23,6</sup> F. PRADA,<sup>36</sup>  
 I. PÉREZ-RÀFOLS,<sup>37</sup> G. ROSSI,<sup>38</sup> L. SAMUSHIA,<sup>39,40,41</sup> E. SANCHEZ,<sup>42</sup> D. SCHLEGEL,<sup>6</sup> M. SCHUBNELL,<sup>43,44</sup> H. SEO,<sup>45</sup>  
 J. SILBER,<sup>6</sup> D. SPRAYBERRY,<sup>14</sup> G. TARLÉ,<sup>44</sup> F. VALDES,<sup>14</sup> B. A. WEAVER,<sup>14</sup> M. WHITE,<sup>46,47</sup> R. ZHOU,<sup>6</sup> AND H. ZOU<sup>48</sup>
- <sup>1</sup>Laboratoire d'Astrophysique, EPFL, 1015 Lausanne, Switzerland  
<sup>2</sup>Department of Astronomy & Astrophysics, The Pennsylvania State University, University Park, PA 16802, USA  
<sup>3</sup>Institute for Gravitation and the Cosmos, The Pennsylvania State University, University Park, PA 16802, USA  
<sup>4</sup>Department of Physics and Astronomy, Purdue University, 525 Northwestern Avenue, West Lafayette, IN 47906, USA  
<sup>5</sup>Physics and Astronomy Department, Rutgers, The State University, Piscataway, NJ 08854, USA  
<sup>6</sup>Lawrence Berkeley National Laboratory, 1 Cyclotron Road, Berkeley, CA 94720, USA  
<sup>7</sup>Department of Physics, Boston University, 590 Commonwealth Avenue, Boston, MA 02215 USA  
<sup>8</sup>Dipartimento di Fisica "Aldo Pontremoli", Università degli Studi di Milano, Via Celoria 16, I-20133 Milano, Italy  
<sup>9</sup>INAF-Osservatorio Astronomico di Brera, Via Brera 28, 20122 Milano, Italy  
<sup>10</sup>Department of Physics & Astronomy, University College London, Gower Street, London, WC1E 6BT, UK  
<sup>11</sup>Institut d'Estudis Espacials de Catalunya (IEEC), c/ Esteve Terradas 1, Edifici RDIT, Campus PMT-UPC, 08860 Castelldefels, Spain  
<sup>12</sup>Institute of Space Sciences, ICE-CSIC, Campus UAB, Carrer de Can Magrans s/n, 08913 Bellaterra, Barcelona, Spain  
<sup>13</sup>Instituto de Física, Universidad Nacional Autónoma de México, Circuito de la Investigación Científica, Ciudad Universitaria, Cd. de México C. P. 04510, México  
<sup>14</sup>NSF NOIRLab, 950 N. Cherry Ave., Tucson, AZ 85719, USA  
<sup>15</sup>Department of Astronomy & Astrophysics, University of Toronto, Toronto, ON M5S 3H4, Canada  
<sup>16</sup>Department of Physics & Astronomy and Pittsburgh Particle Physics, Astrophysics, and Cosmology Center (PITT PACC), University of Pittsburgh, 3941 O'Hara Street, Pittsburgh, PA 15260, USA  
<sup>17</sup>Departamento de Física, Universidad de los Andes, Cra. 1 No. 18A-10, Edificio Ip, CP 111711, Bogotá, Colombia  
<sup>18</sup>Observatorio Astronómico, Universidad de los Andes, Cra. 1 No. 18A-10, Edificio H, CP 111711 Bogotá, Colombia  
<sup>19</sup>Institute of Cosmology and Gravitation, University of Portsmouth, Dennis Sciama Building, Portsmouth, PO1 3FX, UK  
<sup>20</sup>University of Virginia, Department of Astronomy, Charlottesville, VA 22904, USA  
<sup>21</sup>Fermi National Accelerator Laboratory, PO Box 500, Batavia, IL 60510, USA  
<sup>22</sup>Institut d'Astrophysique de Paris. 98 bis boulevard Arago. 75014 Paris, France  
<sup>23</sup>IRFU, CEA, Université Paris-Saclay, F-91191 Gif-sur-Yvette, France  
<sup>24</sup>Center for Cosmology and AstroParticle Physics, The Ohio State University, 191 West Woodruff Avenue, Columbus, OH 43210, USA  
<sup>25</sup>Department of Physics, The Ohio State University, 191 West Woodruff Avenue, Columbus, OH 43210, USA  
<sup>26</sup>The Ohio State University, Columbus, 43210 OH, USA  
<sup>27</sup>Department of Physics, The University of Texas at Dallas, 800 W. Campbell Rd., Richardson, TX 75080, USA  
<sup>28</sup>Department of Physics, Southern Methodist University, 3215 Daniel Avenue, Dallas, TX 75275, USA  
<sup>29</sup>Department of Physics and Astronomy, University of California, Irvine, 92697, USA  
<sup>30</sup>Sorbonne Université, CNRS/IN2P3, Laboratoire de Physique Nucléaire et de Hautes Energies (LPNHE), FR-75005 Paris, France  
<sup>31</sup>Departament de Física, Serra Hünter, Universitat Autònoma de Barcelona, 08193 Bellaterra (Barcelona), Spain  
<sup>32</sup>Institut de Física d'Altes Energies (IFAE), The Barcelona Institute of Science and Technology, Edifici Cn, Campus UAB, 08193, Bellaterra (Barcelona), Spain  
<sup>33</sup>Department of Astronomy, The Ohio State University, 4055 McPherson Laboratory, 140 W 18th Avenue, Columbus, OH 43210, USA  
<sup>34</sup>Institució Catalana de Recerca i Estudis Avançats, Passeig de Lluís Companys, 23, 08010 Barcelona, Spain  
<sup>35</sup>Department of Physics and Astronomy, Siena College, 515 Loudon Road, Loudonville, NY 12211, USA  
<sup>36</sup>Instituto de Astrofísica de Andalucía (CSIC), Glorieta de la Astronomía, s/n, E-18008 Granada, Spain  
<sup>37</sup>Departament de Física, EEBE, Universitat Politècnica de Catalunya, c/Eduard Maristany 10, 08930 Barcelona, Spain  
<sup>38</sup>Department of Physics and Astronomy, Sejong University, 209 Neungdong-ro, Gwangjin-gu, Seoul 05006, Republic of Korea  
<sup>39</sup>Abastumani Astrophysical Observatory, Tbilisi, GE-0179, Georgia

<sup>40</sup>*Department of Physics, Kansas State University, 116 Cardwell Hall, Manhattan, KS 66506, USA*

<sup>41</sup>*Faculty of Natural Sciences and Medicine, Iliia State University, 0194 Tbilisi, Georgia*

<sup>42</sup>*CIEMAT, Avenida Complutense 40, E-28040 Madrid, Spain*

<sup>43</sup>*Department of Physics, University of Michigan, 450 Church Street, Ann Arbor, MI 48109, USA*

<sup>44</sup>*University of Michigan, 500 S. State Street, Ann Arbor, MI 48109, USA*

<sup>45</sup>*Department of Physics & Astronomy, Ohio University, 139 University Terrace, Athens, OH 45701, USA*

<sup>46</sup>*Department of Physics, University of California, Berkeley, 366 LeConte Hall MC 7300, Berkeley, CA 94720-7300, USA*

<sup>47</sup>*University of California, Berkeley, 110 Sproul Hall #5800 Berkeley, CA 94720, USA*

<sup>48</sup>*National Astronomical Observatories, Chinese Academy of Sciences, A20 Datun Road, Chaoyang District, Beijing, 100101, P. R. China*

(Dated: June 18, 2025)

## ABSTRACT

The ubiquity and relative ease of discovery make  $2 \lesssim z \lesssim 5$  Ly $\alpha$  emitting galaxies (LAEs) ideal tracers for cosmology. In addition, because Ly $\alpha$  is a resonance line, but frequently observed at large equivalent width, it is potentially a probe of galaxy evolution. The LAE Ly $\alpha$  luminosity function (LF) is an essential measurement for making progress on both of these aspects. Although several studies have computed the LAE LF, very few have delved into how the function varies with environment. The large area and depth of the One-hundred-deg<sup>2</sup> DECam Imaging in Narrowbands (ODIN) survey makes such measurements possible at the cosmic noon redshifts of  $z \sim 2.4, 3.1, \text{ and } 4.5$ . In this initial work, we present algorithms to rigorously compute the LAE LF and test our methods on the  $\sim 16,000$  ODIN LAEs found in the extended COSMOS field. Using these limited samples, we find slight evidence that protocluster environments either suppress the numbers of very faint and very bright LAEs or enhance medium-bright LAEs in comparison to the field. We also find that the LF decreases in number density and evolves towards a steeper faint-end slope over cosmic time from  $z \sim 4.5$  to  $z \sim 2.4$ .

*Keywords:* Galaxy evolution (594), Luminosity function (942), Spectral energy distribution (2129), High-redshift galaxies (734)

## 1. INTRODUCTION

Ly $\alpha$  emission is one of the primary ways to identify large samples of galaxies in the high-redshift universe (see review by Ouchi et al. 2020). At  $z \gtrsim 2$ , Ly $\alpha$  emission is quite common (Caruana et al. 2018), easily identified via narrow-band imaging (e.g., Gronwall et al. 2007; Ouchi et al. 2008; Ma et al. 2024) or integral-field spectroscopy (e.g., Herenz et al. 2019; Hill et al. 2021), present in galaxies with a very wide range of stellar masses (e.g., Santos et al. 2021; McCarron et al. 2022), and found throughout the  $z \gtrsim 2$  cosmic web (Ramakrishnan et al. 2023). Additionally, clustering analyses of samples of  $2 \lesssim z \lesssim 4$  Ly $\alpha$  emitting galaxies (LAEs) suggest that these objects typically reside in moderate-mass dark matter halos (Gawiser et al. 2007; Guaita et al. 2011; Lee et al. 2014; Ouchi et al. 2018; Herrero Alonso et al. 2021; White et al. 2024), giving them the lowest cluster bias of any galaxy tracer commonly used to probe the high- $z$  universe.

Over the years, a large number of studies have measured the Ly $\alpha$  luminosity function of high- $z$  LAEs, along with the objects' equivalent width distribution (see the compilation by Ouchi et al. 2020). In general, these in-

vestigations have shown a steep rise in the number and luminosity of LAEs going back to redshift  $z \sim 3$ , a “flat” region between  $3 \lesssim z \lesssim 6$ , where little evolution occurs, and then a steep drop at early times ( $z \gtrsim 6$ ). This behavior is most likely linked to the visibility of Ly $\alpha$  photons emitted by a galaxy: at recent epochs, emission can be suppressed by the prevalence of dust, while beyond  $z \sim 6$ , the drop is closely tied to the process of cosmic reionization (Xu et al. 2023)

A major limitation of the programs cited above is the lack of information about galactic environment. An examination of the local universe demonstrates clearly that the morphological and spectral properties of a galaxy depend strongly on the object's location in the cosmic web (e.g., Kraljic et al. 2018; O’Kane et al. 2024; Zarattini & Aguerri 2025). But whether the same is true for LAEs at high redshift is an open question. Until recently, most LAE studies did not have the sky coverage, depth, sampling density, and/or redshift resolution to enable robust estimates of galactic environment. Nevertheless, simulations show that LAEs are excellent tracers of large scale structure (Im et al. 2024; Lee et al. 2024), meaning that with a large enough survey, we should be able to quantify the impact of environment on LAE science.

ODIN, the One-hundred-deg<sup>2</sup> DECam Imaging in Narrowbands survey, is a large NOIRLab program which is using the Dark Energy Camera (DECam) on the Blanco 4 m telescope at the Cerro Tololo Inter-American Observatory to identify  $z = 2.4, 3.1,$  and  $4.5$  LAEs over seven extremely wide southern-hemisphere and equatorial fields (Lee et al. 2024). ODIN’s goal is to observe  $\sim 2.3 \times 10^8$  cMpc<sup>3</sup> of space around cosmic noon and create large samples of the epochs’ richest protoclusters (tens to hundreds), Ly $\alpha$  blobs (thousands), and LAEs ( $\sim 150,000$ ).

In this paper, we describe a pilot survey which uses ODIN observations of one field – the  $\sim 9$  deg<sup>2</sup> Extended COSMOS region – to determine how the Ly $\alpha$  emission-line luminosity function changes as a function of galaxy density. In Section 2, we describe the observations used to detect the LAEs and their selection effects; in Section 3 we detail the methodology used to determine the LAE luminosity function, and in Section 4 we present our results. We conclude by discussing the implications of this first-look survey.

Throughout this paper, we assume a  $\Lambda$ CDM cosmology with  $\Omega_\Lambda = 0.73$ ,  $\Omega_M = 0.27$  and  $H_0 = 70$  km s<sup>-1</sup> Mpc<sup>-1</sup> (Bennett et al. 2013). All magnitudes given in the paper are in the AB magnitude system (Oke 1974). All data shown in the figures will be made available upon publication.

## 2. DATA AND SELECTION EFFECTS

ODIN observations in and around the COSMOS region were performed in two rings, and covered a  $\sim 9$  deg<sup>2</sup> region of the sky. As described by Lee et al. (2024), DECam images were acquired in three narrow-band filters: N419 (central wavelength and full-width at half-maximum of  $\lambda_c = 4193$  Å, FWHM = 75 Å), N501 ( $\lambda_c = 5014$  Å, FWHM = 76 Å), and N673 ( $\lambda_c = 6750$ , FWHM = 100 Å). Counterpart broadband *grizy* images were taken from the Hyper Suprime-Cam Subaru Strategic Program (HSC-SSP; Aihara et al. 2018, 2019), and reached significantly deeper than the narrow band data. Summaries of the depths of the ODIN and HSC observations are given in Table 1 and 2.

The dithered narrow-band images were reduced and calibrated in the standard manner using the DECam Community Pipeline (Valdes et al. 2014). This pipeline begins by removing detector overscan, bias, cross-talk, and non-linearities, and then applying corrections for the dome flatfield, pupil illumination, and CCD fringing. The pipeline then subtracts the background, calculates astrometric solutions from the field stars, remaps each frame onto a common coordinate system, applies the night’s photometric zero-point, stacks the frames with

**Table 1.** COSMOS ODIN Images

Band	No. of Exp	Single Exp Time (s)	$z_c^a$	$\Delta z^a$	Seeing	$5\sigma$ Depth
N419	126	1200	2.449	0.061	1.19''	25.37
N501	72	1200	3.124	0.062	1.04''	25.37
N673	169	1110	4.553	0.082	1.03''	25.68

<sup>a</sup>  $z_c$  and  $\Delta z$  represent the Ly $\alpha$  redshifts for the central wavelength and FWHM of the narrow-band filter.

**Table 2.** HSC Images

Band	Seeing	$5\sigma$ Depth (Deep/UltraDeep)
<i>g</i>	0.85''	26.5/27.1
<i>r</i>	0.74''	25.9/26.4
<i>i</i>	0.66''	25.6/26.2
<i>z</i>	0.63''	25.5/26.0
<i>y</i>	0.75''	24.9/25.4

outlier rejection, and finally masks artifacts produced to bad-pixels, saturated stars, cosmic rays, satellite trails, and the like.

The process of identifying LAE candidates in COSMOS is described in Firestone et al. (2024). In brief, the Source Extractor image analysis program (Bertin & Arnouts 1996) is run in dual image mode, and the fluxes of objects identified in the DECam narrow-band images are compared to their counterparts in the HSC-SSP data. Those sources satisfying the seven selection criteria enumerated by Firestone et al. (2024) are then classified as LAE candidates. These criteria include requiring the LAEs to have a flux excess in the narrow-band, satisfy two different signal-to-noise constraints, survive cuts in half-light radius and total magnitude to exclude local objects, and have consistent magnitudes on image half-stacks. (This last step is effective for removing contamination by transients and moving objects.) The process produced samples of 6100 LAE candidates in the N419 band, 5782 in N501, and 4101 in N673.

To convert the narrow-band AB magnitudes of our LAE candidates into Ly $\alpha$  fluxes, we first removed the underlying continuum from each LAE using the object’s broadband flux densities and the prescription given by Firestone et al. (2024). We then translated the remaining AB flux density into Ly $\alpha$  flux using

$$F_{\text{Ly}\alpha} = 3.63 \times 10^{-20} 10^{-m_{\text{AB}}/2.5} \frac{c}{\lambda^2} \frac{\int T_{\lambda} d\lambda}{T_C} \quad (1)$$

where we assign  $T_C$  to be the maximum transmission of the filter curve, ( $T_{\lambda}$ ) (Jacoby et al. 1987; Gronwall et al. 2007).

Figure 1 shows the raw LAE flux distribution in each filter. The galaxies below a given flux threshold (approximately the 50% completeness limit) are shown in light gray while those objects above our bright flux limit (see § 2.1 and § 2.2 for details) are shown in gold. Neither set is included in our luminosity function calculations. In all three filters, the data lying between these two limits span a little over one dex in emission-line flux.

### 2.1. Completeness and Survey Depth

As detailed in Lee et al. (2024) and summarized in Table 1, the ODIN data were acquired via a large number of individual exposures organized in a two-ring dither pattern designed to cover a  $\sim 9.5 \text{ deg}^2$  region as uniformly as possible. The resulting depth of this pattern was mapped by Ramakrishnan et al. (2023) by placing  $2''$  apertures randomly over the field and measuring their  $5\sigma$  noise fluctuations. These data confirmed that the survey depth is radially symmetric, is roughly constant over the region’s inner  $1.5^\circ$ , and then declines smoothly at larger radii.

Figure 2 illustrates this behavior by showing completeness versus magnitude and radial distance for our co-added N501 image. We assess the completeness of our LAE sample as a function of position and narrowband magnitude by injecting mock narrowband sources into our science images and evaluating their recovery. The process of injecting mock sources essentially proceeds in three steps: the creation of a noiseless, deconvolved source image; convolution of the source image with the narrowband PSF; and addition of the convolved image to our science image to introduce realistic noise. In order to create an initial source image, mock sources are assigned a narrowband magnitude, uniformly distributed between magnitudes 21 and 26 (AB). The magnitude is converted to flux using the zeropoint of the science image, and the entirety of this flux is assigned to a single pixel, as the majority of LAEs are expected to be point sources in our images. The source image is convolved with a 2D Gaussian with FWHM 1 arcsec (3.7 pixels), and the convolved image is added to the science image. We then run SExtractor to recover the mock sources, using identical settings to those used to build our narrowband catalog for LAE selection.

The full field of view of the ODIN data is a circular region with radius  $\approx 1.9 \text{ deg}$  (see Lee+2024). We divide

this area into  $9 \times 9$  ‘patches’ with  $\approx 36 \text{ arcmin}$  to a side. The injection and recovery of sources into each patch is done independently, in order to measure the completeness as a function of position.

### 2.2. AGN and other Contaminants

While Firestone et al. (2024) have developed sensitive algorithms for LAE classification, the combination of narrow-band and broad-band data cannot be a perfect discriminator. We have used data from the Dark Energy Spectroscopic Instrument (DESI) survey (DESI Collaboration et al. 2022) to test whether the LAE candidates identified by ODIN are indeed LAEs at the redshifts targeted by the narrow-band filters.

DESI is a large spectroscopic survey with a state-of-the-art fiber network capable of measuring 5000 spectra simultaneously (DESI Collaboration et al. 2016a,b; Silber et al. 2023; Poppett et al. 2024), designed to study the properties of dark energy (Levi et al. 2013). The spectra of DESI are accompanied by significant imaging (Dey et al. 2019), and data acquisition and reduction are streamlined with various software pipelines (e.g., Guy et al. 2023; Schlafly et al. 2023). Survey strategies have been improved with a 5-month validation campaign (DESI Collaboration et al. 2024a). An early data release (DESI Collaboration et al. 2024b) as well as a first full release (DESI Collaboration et al. 2025a) are publicly available, and several papers have analyzed this data (DESI Collaboration et al. 2024c,d,e; Adame et al. 2025a,b,c). For this study, we have used spectra from the first and second data releases (DESI Collaboration et al. 2025a,b).

In total, DESI spectra exist for 2783 of ODIN’s LAE candidates – 1279 at  $z \sim 2.4$  (N419), 1410 at  $z \sim 3.1$  (N501), and 94 at  $z \sim 4.5$  (N673). Each spectrum was examined and placed into one of four categories: confirmed LAEs with no AGN activity (82%), AGN identified via their broad Ly $\alpha$  line (1%), foreground contaminants, which are generally AGN detected via their C IV  $\lambda 1549$  or C III]  $\lambda 1909$  emission (6%), or undetermined (11%). The latter refers to spectra that are too difficult to classify. The analysis of DESI-ODIN spectra will be published in Dey et al. (in prep). These data confirm that in general, the ODIN LAE samples are quite pure: integrated over all magnitudes and removing the undetermined sources from consideration (as we do not know what fraction of such sources are LAEs), the contamination rates for the candidates at all three redshifts are  $\sim 7\%$ . Table 3 shows the detailed demographics for the DESI comparison.

Even with low contamination rates, no narrow-band survey can be completely free of interlopers, and at the

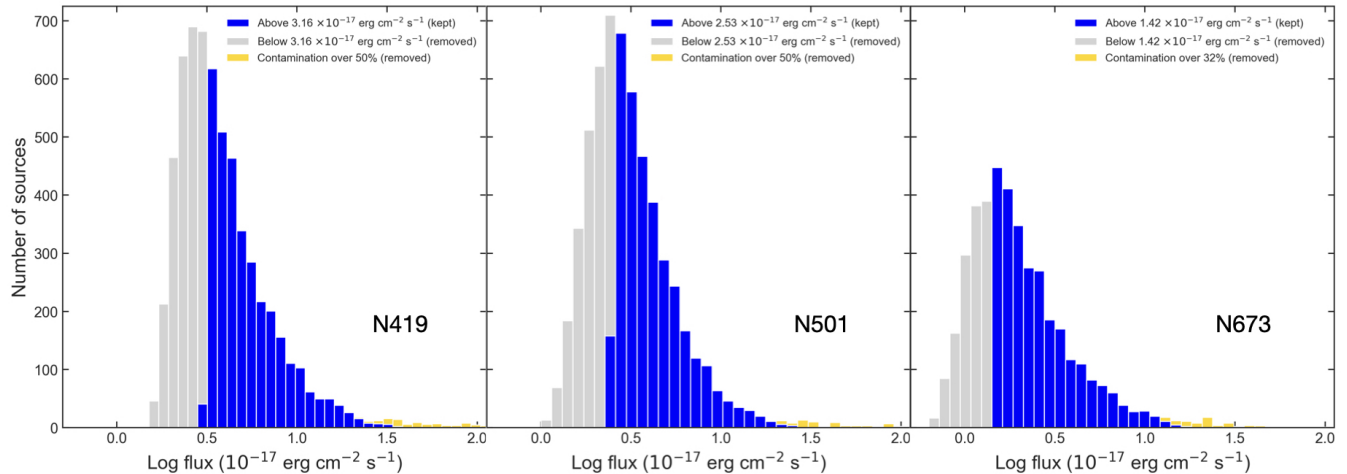


**Figure 1.** Raw emission-line flux distributions in each of the three narrow-band filters. The sample of galaxies used in the luminosity function calculations are shown in blue. Galaxies with fluxes below a certain value—approximately the 50% completeness level—are colored light gray, while very bright objects that are likely foreground contaminants are colored gold. The useful data cover  $\sim 1.1$  dex in flux.

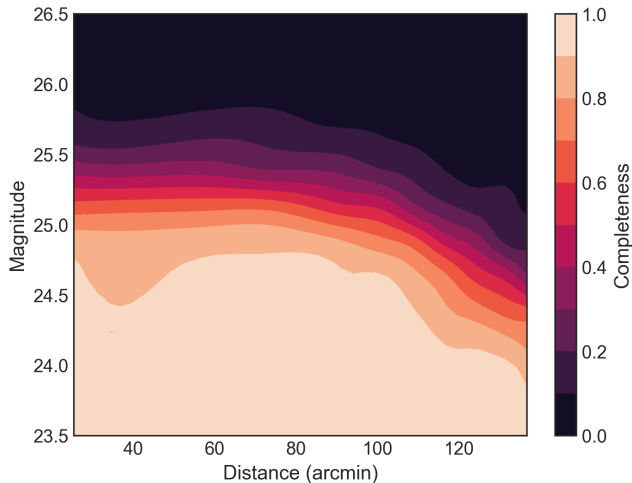


**Figure 2.** Completeness as a function of N501 magnitude and radial distance from the center of the COSMOS field. Within the field’s inner  $1.5^\circ$  core, the variations in survey depth are small. However, at the extreme edge of the field, the survey depth is  $\sim 0.5$  mag shallower than in the center.

**Table 3.** ODIN-DESI Spectral Sample Demographics

Filter	Normal LAE	Broad-line LAE	Foreground Contaminant	Undetermined
N419	1017	21	57	184
N501	1205	13	79	113
N673	81	1	6	6

of contaminants can have an out-sized effect on the fitted luminosity function. To quantify the purity of our LAE samples as a function of brightness, we grouped the sources into 10 evenly spaced magnitude bins (4 bins for N673 given the dearth of spectra), and in each bin, we found the fraction of normal (non-AGN) LAEs compared to the total number of objects with classifiable spectra. Bins with no available DESI spectra (at the faint end) were assigned a purity of 1 (no contamination) to avoid biasing the results with a poorly informed extrapolation. This purity function, shown in Figure 3, represents the fraction of confirmed LAEs in N419, N501, and N673. Given the spectral demographics quoted above, the inclusion or exclusion of the undetermined sources has little effect on the shape of this function.

In theory, there are two ways to handle the effect of contamination in our sample. The first involves modeling the putative luminosity function of the foreground interlopers and subtracting this model from the LAE sample. Although this simple strategy has some advantages, we prefer the more elegant solution of treating contaminants as a form of “overcompleteness” in the LAE number counts. For example, if the fraction of sources that are truly LAEs at a given magnitude is 0.5, then the completeness at that magnitude is  $1/0.5$ , or 200%, and the observed number counts must be divided by two to reflect the intrinsic population. Doing this allows us to combine our measurements of photometric incompleteness (i.e., Figure 2) and contamination into a single multiplicative correction function that we can apply throughout the field.

bright end of the luminosity function, a small number

Figure 4 shows a selection of these curves for the N419, N501, and N673 data. As expected, the values at the bright end of the function exceed 1.0: At these luminosities, photometric incompleteness is negligible and all curves are defined by the inverse of the purity functions given in Figure 3. We artificially truncate these curves at 2.0 (1.5 for N673), which means that we exclude all data where the correction for contamination is more than a factor of two. The cap prevents the uncertainties associated with the bright end of our completeness curves from dominating our solutions. Conversely, at faint luminosities, the sample purity approaches 1, but the survey’s photometric completeness is declining rapidly. In this regime, the behavior of the curves reflects the effect of the ODIN dithering pattern (see Figure 1 of Ramakrishnan et al. 2023). Once again, to prevent completeness uncertainties from dominating our solutions, we limit our analysis to locations where our corrections are greater than 0.5 for N419 and N501 and greater than 0.32 for N673 since the small number of spectra does not allow us to properly probe the very bright end.

### 2.3. Continuum Considerations

A subtle but important point to note is that our measurements of photometric completeness and contamination have been performed as a function of narrow-band magnitude. This is perfectly reasonable since magnitudes are what are recorded by the Source Extractor program and our completeness corrections are tied directly to these measurements. Given our treatment of contamination, it makes sense to use narrow-band magnitudes here as well, as it greatly simplifies the analysis.

However, the goal of our study is to measure the Ly $\alpha$  luminosity being emitted from ODIN sample of LAEs. This requires the extra step of removing an LAE’s continuum emission, also present in the filter. The continuum subtraction can introduce an error into our contamination measurements.

For example, by definition ODIN LAEs have rest-frame equivalent widths larger than 20 Å. Given the FWHM values of the N419, N501, and N673 filters, this means that the recorded flux density through our narrow-band filters can be up to a factor of  $\sim 2$  greater than that associated with the Ly $\alpha$  emission line alone. More typically, if we adopt the ODIN LAE equivalent width distributions found by Firestone et al. (2024), then we should expect the Ly $\alpha$  emission line to be on average  $\sim 1.3$  times fainter than the flux implied by the narrow-band filter alone.

This behavior is confirmed in Figure 5, which compares the raw and continuum-subtracted line fluxes of

our N501 LAEs. The correlation between the two quantities is clear, as is the scatter produced by the distribution of LAE equivalent widths.

While it is possible to fold information about an LAE’s equivalent width into the completeness and purity measurements, the computational cost of such an analysis is excessive, increasing the running time by over an order of magnitude. Instead, to fit our Ly $\alpha$  emission-line luminosity functions using narrow-band magnitude-based completeness curves, we relate the two quantities using an orthogonal-regression best-fit line. The simple procedure avoids biasing our luminosity function integrals (§ 3.3) and minimizing any systematic introduced by the issue. These best-fit lines are

$$\begin{aligned} f_{\text{NB}} &= 1.47 f_{\text{line}} - 0.30 & (\text{N419}) \\ f_{\text{NB}} &= 1.37 f_{\text{line}} - 0.21 & (\text{N501}) \\ f_{\text{NB}} &= 1.36 f_{\text{line}} - 0.09 & (\text{N673}) \end{aligned} \quad (2)$$

## 3. METHODOLOGY

### 3.1. The Preliminaries

The luminosity function is an important quantity detailing the distribution of objects in the universe and as such, there is an abundance of literature describing various techniques for its computation (e.g., Schmidt 1968, 1970; Lynden-Bell 1971; Huchra & Sargent 1973; Avni & Bahcall 1980). Here, we follow the methodology of Ciardullo et al. (2013) and Nagaraj et al. (2023), but modify their equations to reflect the nature of the ODIN narrow-band survey.

We begin by describing the difference between the true, intrinsic Ly $\alpha$  luminosity function of LAEs ( $\phi$ ) and the observed function ( $\phi'$ ). The latter is modified by observational effects, such as completeness, contamination, photometric errors, and quirks associated with the survey filter’s transmission curve.

As described in § 2.2, the first two of these effects are closely related. Photometric incompleteness, whose dependence on position is shown in Figure 2, removes galaxies from the faint end of the luminosity function (i.e., these galaxies are not observed), and thus requires that the observed number of LAE candidates be boosted to recreate the true number. Conversely, contamination by AGN and other interlopers, as illustrated in Figure 3, artificially adds objects to (primarily) the bright end of the luminosity function and causes a form of overcompleteness. Here we treat incompleteness and contamination in exactly the same manner using a luminosity-dependent multiplicative correction to the observed number density of LAE candidates.

Next we consider the effect that photometric measurement uncertainties have on the luminosity function.

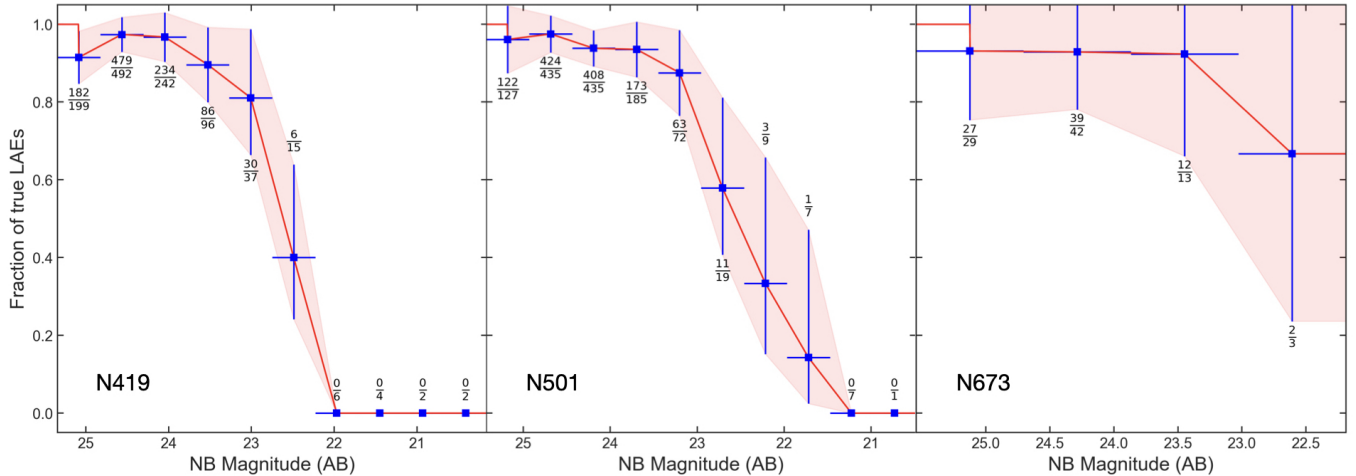


**Figure 3.** Fraction of ODIN sources that are spectroscopically confirmed LAEs as a function of narrow-band magnitude in the N419 (left), N501 (middle), and N673 (right). The error bars represent Poisson uncertainties. (These error bars are generally not incorporated into the analysis due to computational and algorithmic constraints.) The N673 data suffers from a relative dearth of confirming spectroscopy, limiting our ability to measure the function. Integrated over all magnitudes, the confirmed fraction of LAEs is over 90% in all three filters. However, at magnitudes brighter than  $m_{AB} \sim 24$ , the purity fraction declines rapidly, and is near zero at  $m_{AB} \sim 22$  in N419 and N501. The ratio of confirmed LAEs to total ODIN-DESI spectra per bin is displayed above or below each point. We multiply the reciprocal of this function by our photometric completeness curves to determine the effective completeness at each location in the survey.

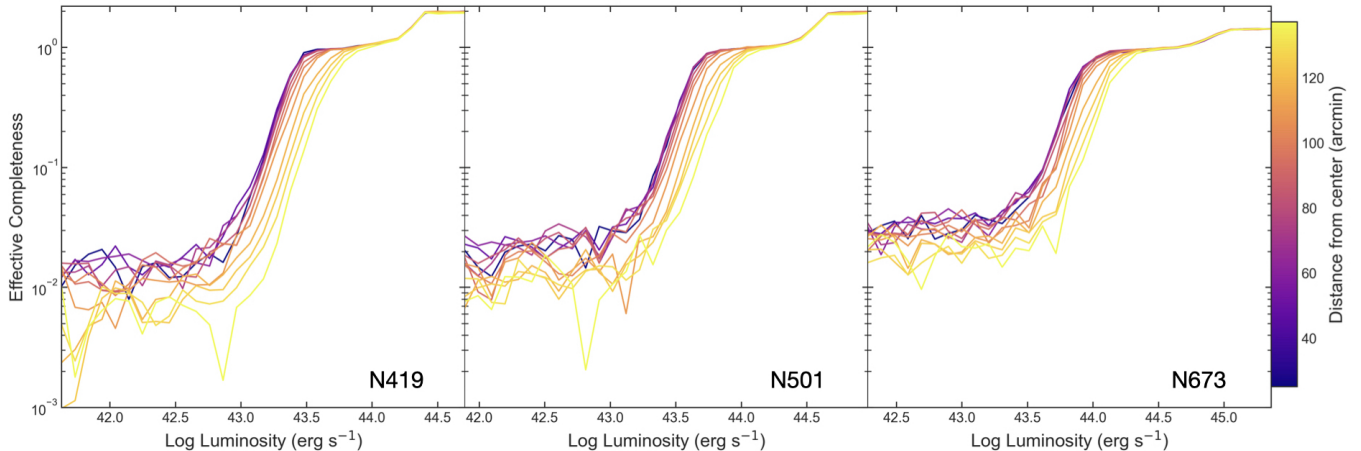


**Figure 4.** Effective completeness as a function of luminosity (x-axis) and distance (line color) from center of the Extended COSMOS field for N419 (left), N501 (middle), and N673 (right). As described in the text, these curves are the product of photometric completeness, as determined through simulations, and “overcompleteness” caused by the inclusion of AGN and other foreground interlopers.

There are two ways to address this problem: One can convert the observed luminosity function,  $\phi'$ , to the true luminosity function  $\phi$  via the application of an [Eddington \(1913, 1940\)](#) correction, or one can change  $\phi$  into  $\phi'$  by convolving the true function with a Gaussian kernel representing the dataset’s photometric error as a function of luminosity ([Mehta et al. 2015](#)). Both methods have drawbacks: the Eddington correction requires a stable measurement of the observed luminosity function’s second derivative, while convolutions are gener-

ally computationally expensive. In our case, including the error convolutions increase the execution time by factors of 20 to 30. Fortunately, the effect of photometric uncertainties on the luminosity function of our narrow-band selected LAE candidates is quite minor: at the bright-end the function, the photometric errors are minimal, while at the faint-end, their effect is dwarfed by issues associated with incompleteness. Thus we ignore the term, as its omission has a negligible impact on our results.

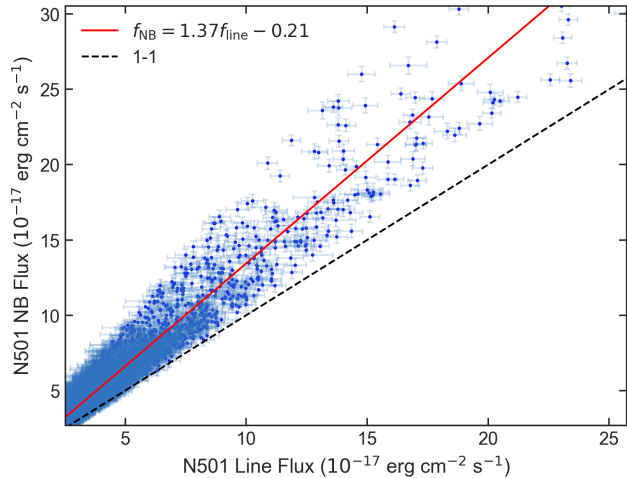


**Figure 5.** Total narrow-band flux recorded in the N501 filter versus Ly $\alpha$  flux for ODIN LAEs in the Extended COSMOS field. The orthogonal-regression best-fit line is shown in red; this line is consistent with that expected from the LAE’s equivalent width distribution and the filter’s FWHM. We use this relation to approximate the relation between line and narrow-band flux when computing integrals for the luminosity function. For reference, we also provide the 1-1 relation as a black dotted line.

Finally, we examine how the transmission curves of ODIN’s narrow-band filters affect the recorded luminosity function. As illustrated in the left-hand panel of Figure 6, the filters used by ODIN do not have perfectly rectangular transmission functions—when placed in the converging beam of a fast telescope, even the best top-hat filters will have non-negligible wings (Eather & Reasoner 1969). As a result, galaxies with emission lines that fall onto the wings of the transmission curve have their fluxes underestimated (or even fade below the completeness limit), since the throughput at those wavelengths is less than that at the center of the filter.

The non top-hat shape of a narrow-band filter’s transmission curve not only creates some uncertainty in the translation of observed flux to Ly $\alpha$  luminosity but also plays a role in calculating the effective volume of the survey. The most luminous Ly $\alpha$  emitters will be detectable even if their redshift places their emission on the wings of an interference filter’s transmission curve, hence the volume for their detection is relatively high. Conversely, galaxies with weak Ly $\alpha$  will only be seen if their emission line lies on a filter’s top-hat region, lowering their survey volume. This effect for the N501 filter is shown in the middle panel of Figure 6.

There are two ways to handle this issue. The first method, in which the effect of the filter bandpass is reproduced via Monte Carlo simulations, was pioneered by Shimasaku et al. (2006) and has recently been used by

Sobral et al. (2018); we use it below in our calculation of the non-parametric luminosity function. The second method involves convolving the true luminosity function with a kernel derived from the filter transmission curve,

$$G(\Delta\mathcal{L})d\Delta\mathcal{L} = C_T \left[ \left\{ \left| \frac{d\lambda}{d\Delta\mathcal{L}} \right| d\Delta\mathcal{L} \right\}_{\text{blue}} + \left\{ \left| \frac{d\lambda}{d\Delta\mathcal{L}} \right| d\Delta\mathcal{L} \right\}_{\text{red}} \right] \quad (3)$$

(Gronwall et al. 2007). In the above equation,  $C_T$  normalizes the kernel to unity and  $\Delta\mathcal{L} \equiv \log T_C - \log T(\lambda)$ , where  $T(\lambda)$  is the filter’s transmission as a function of wavelength and  $T_C$  is the max transmission. In particular,  $\Delta\mathcal{L}$  is the difference in log luminosity between the observed and intrinsic luminosity. Note that because an underestimated luminosity can be produced by emission lines at either wing of the transmission curve, this kernel includes contributions from both the blue and red sides of the filter. The shape of this kernel is displayed in the right panel of Figure 6. We use this method when fitting the luminosity function with our maximum-likelihood estimator.

When the effects of completeness, contamination, and non-uniform filter transmission are taken into account, the equation relating the observed luminosity function to the true function is

$$\phi'(\mathcal{L}, \hat{n}) = p(\mathcal{L}_{\text{NB}}, \hat{n}) [F * \phi(\mathcal{L})] \quad (4)$$

where  $p(\mathcal{L}_{\text{NB}}, \hat{n})$  is the effective completeness at each position  $\hat{n}$  and evaluated at narrow-band log luminosity  $\mathcal{L}_{\text{NB}}$  (see § 2.3 for details). For simplicity, in subsequent equations we will use  $\mathcal{L}$  for effective completeness, although it is understood that completeness is evaluated using the narrow-band magnitudes data and converted to log line luminosity using equation 2. Then,  $F$  is the convolution kernel representing the filter transmission effects. In the sections that follow, we avoid numerical issues by performing our calculations using log rather than linear Ly $\alpha$  luminosity, i.e.,  $\mathcal{L} \equiv \log L$  and fit the luminosity distribution both non-parametrically and via the Schechter (1976) function

$$\phi(\mathcal{L}, z) = \ln(10) 10^{\log \phi_* 10^{[\mathcal{L} - \mathcal{L}_*][\alpha + 1]}} \exp(-10^{\mathcal{L} - \mathcal{L}_*}) \quad (5)$$

with  $\alpha$ ,  $\mathcal{L}_*$ , and  $\log \phi_*$  representing the function’s faint-end slope, bright-end cutoff, and normalizing constant, respectively.

For the rest of section, we delve into the details of computing the luminosity function. We first use a non-parametric approach that corrects for the effects of the filter curve using a post-processing empirical correction.

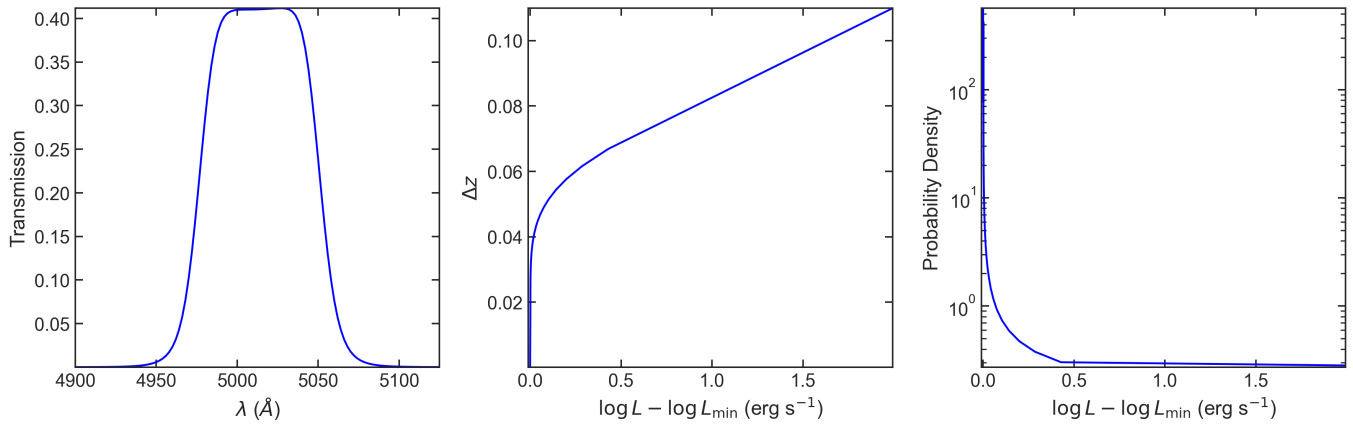


**Figure 6.** The properties of the N501 filter curve used by ODIN. The N419 and N673 filter behave in a similar fashion. Left: the transmission curve of the filter. Middle panel: the filter’s effective redshift width as a function of emission-line luminosity. The value of  $L_{\min}$  is taken as roughly the 50% completeness level since below that limit is where we stop using sources for calculations. Bright objects can be detected even if their redshift places them on the filter’s wings. Right: the convolution kernel  $G(\Delta\mathcal{L})$  used to convert the true luminosity function into the observed function.

We then pivot to a maximum likelihood analysis that incorporates the filter effects using the kernel defined in Equation 3. The first method has the advantage of rapid calculation and does not force the function to fit any preconceived form. However, its results can be affected by how the data are divided into bins of luminosity, and therefore may be less accurate. The second method assumes that the LAE luminosities follow the form of a Schechter (1976) function and is computationally more demanding. However, it does not force galaxies into bins and its results are more easily compared to those of other surveys.

### 3.2. Computing the Non-Parametric Luminosity Function

If we ignore the filter corrections for the moment and only add them later as an empirical correction, we can calculate the Ly $\alpha$  luminosity functions of ODIN LAEs using the  $V_{\text{eff}}$  method, which is fully described in § 3.2 of Nagaraj et al. (2023). This procedure, which is a slightly more complex version of the well-known  $1/V_{\text{max}}$  method (Schmidt 1968, 1970; Huchra & Sargent 1973; Avni & Bahcall 1980), computes the number density of galaxies in a series of log-luminosity bins via

$$\phi_i^{-1} = \Delta z \left. \frac{dV}{dz d\Omega} \right|_{z_0} \Omega_0 p(\mathcal{L}_i) \equiv V_{\text{eff}}(\mathcal{L}_i) \quad (6)$$

where  $\phi_i$  is the true number density of galaxies in luminosity bin  $i$ ,  $\Delta z$  is the effective redshift width of the filter,  $p_i(\mathcal{L})$  is the applicable completeness fraction for that bin, and  $\Omega_0$  is the total area of the survey. Using this procedure we calculate  $\phi_i$  for all galaxies and average the results in 50 bins in log luminosity space. We then use the bootstrap method to estimate the errors:

we sample our set of luminosities 100 times (with sample sizes equal to the total number of sources but selected with replacement), recalculate the luminosity function, and determine the variance in the 100 results.

To account for the non-top-hat filter effects, we follow the prescription given by Sobral et al. (2018).

1. We adopt the luminosity function derived from the  $V_{\text{eff}}$  method without any filter transmission effects, and randomly draw a large number (2.5 million) of LAEs from that distribution.
2. We assume that the LAEs observed through our narrow-band filter occupy a uniform distribution in redshift space that reaches far into the wings of the transmission filter. In our case, we distribute galaxies out to twice the effective width of the filter to include essentially all of the galaxies that could have measurable flux without having unphysically large intrinsic luminosities.
3. We multiply the line luminosities of the mock LAEs by the  $T(\lambda)/T_C$  value appropriate to the galaxies’ redshifts to mimic the line flux that would be observed.
4. We define the effective redshift width  $\Delta z$  as the average redshift interval within which each luminosity could be observed (see the middle panel of Figure 6).
5. We use the  $V_{\text{eff}}$  method (Equation 6) to calculate the luminosity function for both the original and transmission-corrected distributions of galaxies.

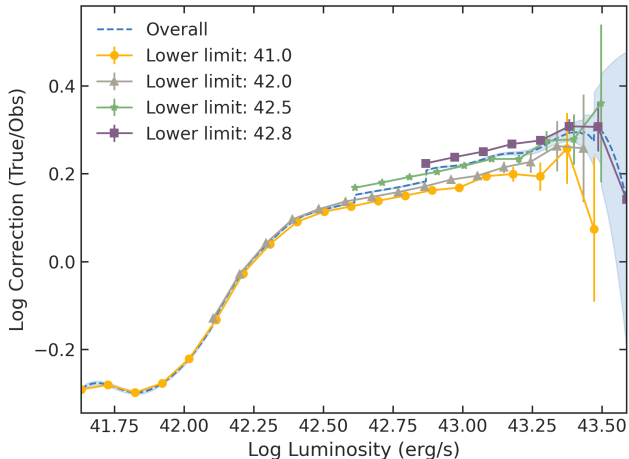


**Figure 7.** The log correction factor as a function of luminosity for the Monte Carlo experiments used to determine the effect that the N501 filter transmission curve has on the  $V_{\text{eff}}$  method. The overall correction is taken as a weighted average of the individual experiments. The  $1 - \sigma$  uncertainties on the correction are shown in light blue. The correction increases monotonically from  $\log L \approx 41.8$  to  $\log L \approx 43.4$ . Since our N501 data only goes down to  $\log L \gtrsim 42.3$ , only the corrections above this limit are used.

6. We measure the ratio of the luminosity functions to determine the corrections required to account for filter transmission effects.
7. As a check, we apply the corrections to the original luminosity function and repeat the analysis (once). If the corrections are accurate, this process recovers the original luminosity function. We find this to be the case.

In practice, the results of our Monte Carlo simulations are highly volatile at the high-luminosity end ( $\mathcal{L} > \mathcal{L}_*$ ) due to the small number of extremely bright sources. Thus, we had to repeat the experiment using several different minimum luminosity values (41.0, 42.0, 42.5, 42.8) and splice the results together, as shown in Figure 7. (The higher the minimum luminosity, the higher the fraction of high-luminosity objects in the simulation.) The overall correction was taken as a weighted sum of the interpolations of the different experiments within the given luminosity ranges (i.e., no extrapolations were used). The reciprocal of the (interpolated) standard deviation in each experiment’s correction factor was taken as the weighting factor.

The correction factor increases monotonically with log luminosity from  $\mathcal{L} \approx 41.8$  to  $\mathcal{L} \approx 43.4$ , i.e., the full range encompassed by the data. Above this value, the results are volatile, as the rapidly declining luminosity function takes its toll on the number of galaxies detected.

Conversely, at the faint end of the distribution, the effects of the transmission curve are complex because of the balancing act between bright galaxies with redshifts that place them on the wings of the interference filter, fainter galaxies that are distributed throughout the filter (and sometimes fall below the completeness limit), and the differential volume effect. Our corrections are similar to those found in Sobral et al. (2018), due to the similarity in the filter transmission curves.

### 3.3. Fitting the Luminosity Function

We fit the unbinned set of observed LAE Ly $\alpha$  line luminosities using the maximum likelihood technique developed by Ciardullo et al. (2013) and Nagaraj et al. (2023). Given Poisson statistics, we can write the likelihood (denoted as  $\mathcal{P}$ ) of any observed luminosity function  $\phi'(\mathcal{L}, z, \hat{n})$  fitting a set of Ly $\alpha$  luminosities as

$$\ln \mathcal{P}_{\alpha, \mathcal{L}_*, \phi_*} = \sum_i^N \ln \phi'(\mathcal{L}_i, z_i, \hat{n}_i) - \int_{\Delta\Omega} \int_{z_1}^{z_2} \int_{\mathcal{L}_{\min}(z, \hat{n})}^{\infty} \phi'(\mathcal{L}, z, \hat{n}) \frac{dV}{dz d\Omega} d\mathcal{L} dz d\Omega \quad (7)$$

where  $N$  is the number of galaxies in the sample,  $\mathcal{L}_{\min}$  is the cutoff luminosity below which we ignore all observations (here taken to be the luminosity corresponding roughly to 50% completeness),  $\Delta\Omega$  is the solid angle covered by the survey,  $\frac{dV}{dz d\Omega}$  is the differential volume element, and  $z_1$  and  $z_2$  are the redshift limits that reach sufficiently far into the wings of the transmission curve to include all the detected galaxies.

In our calculation of  $\phi'$ , we ignore the photometric error convolution of Equation 4, as it is computationally expensive and has almost no effect on the final result (see § 3.1). We also truncate the filter transmission convolution kernel at  $10^{-2}$  of the peak transmission (i.e.,  $\Delta\mathcal{L} = 2.0$ ), as a galaxy’s emission would have to be very large in order to have its Ly $\alpha$  line visible at 1/100th of its true flux. Finally, we treat the top-hat region of the transmission curve (where Equation 3 is indeterminate) as a Dirac Delta function, whose integral over  $\Delta\mathcal{L}$  is the fraction of wavelength space the top-hat occupies compared to the entire transmission curve down to  $\Delta\mathcal{L} = 4.0$ . The resultant convolution kernel for the N501 filter is shown in the right panel of Figure 6.

It is computationally expensive to calculate the likelihoods produced by Equation 7 for the hundreds of thousands of iterations needed to obtain statistically viable results from Markov Chain Monte Carlo (MCMC) sampling. However, if we decouple the likelihood calculations for  $\alpha$  and  $\mathcal{L}_*$  from that of the normalization parameter  $\phi_*$ , we can recover the results of Equation 7 in a fraction of the execution time.

To do this, we ignore the photometric error convolution and expand Equation 4 to

$$\phi'(\mathcal{L}, \hat{n}) = A p(\mathcal{L}, \hat{n}) \int_{\mathcal{L}_{\min}}^{\mathcal{L}_{\min} + \Delta\mathcal{L}} \phi_{\text{true}}(\mathcal{L}') G(\mathcal{L}' - \mathcal{L}) d\mathcal{L}' \quad (8)$$

where  $\mathcal{L}_{\min}$  is the minimum observable log luminosity at the central redshift averaged over radial distance from the center of the field,  $\Delta\mathcal{L} = 4$  as described above, and  $A$  is chosen such that  $\int_{\mathcal{L}_{\min}}^{\infty} \phi'(\mathcal{L}) d\mathcal{L} = 1$ . For a given combination of  $\alpha$  and  $\mathcal{L}_*$ , we use the curves of Figure 4 to map out the variations of the assumed Schechter function versus position in the survey field. The likelihood that our galaxy sample is drawn from this  $\phi'(\mathcal{L}, \hat{n})$  distribution is then

$$\ln \mathcal{P}_{\alpha, \mathcal{L}_*} = \sum_{i=1}^N \ln \phi'_{\alpha, \mathcal{L}_*}(\mathcal{L}_i, \hat{n}_i) \quad (9)$$

These likelihoods are calculated over a grid of  $101 \times 101$  uniformly-spaced  $\alpha$  and  $\mathcal{L}_*$  values, with the limits of the grid given in Table 4. We will come back to this grid later in the section.

Next, we calculate the likelihood for each value of  $\phi_*$ . To do this, we integrate  $\phi'$  over luminosity, survey area, and redshift to get the expected number of observed galaxies for each assumed value of  $\alpha$ ,  $\mathcal{L}_*$ , and  $\phi_*$ , i.e.,

$$N_{\alpha, \mathcal{L}_*}(\phi_*) = \int_{z_{\min}}^{z_{\max}} \int_{\Delta\Omega} \int_{\mathcal{L}_{\min}(z, \hat{n})}^{\mathcal{L}_{\max}(z)} p(\mathcal{L} + \log T_{\text{frac}}(z), \hat{n}) \times \phi_{\text{true}, \alpha, \mathcal{L}_*}(\mathcal{L} | \phi_*) \frac{dV}{dz d\Omega}(z) d\mathcal{L} d\Omega dz \quad (10)$$

where  $T_{\text{frac}}(z) = T(\lambda)/T_C$  for the wavelength corresponding to Ly $\alpha$  at redshift  $z$ . If we make the very good assumption that the survey area is circular with radius  $R$  (such that the area is 10 deg<sup>2</sup> with a filling factor of 90%, leading to the effective area of 9 deg<sup>2</sup>), and the completeness versus radius dependence are those plotted in Figure 4, this equation simplifies to

$$N_{\alpha, \mathcal{L}_*}(\phi_*) = 2\pi \int_{z_{\min}}^{z_{\max}} \int_0^R \int_{\mathcal{L}_{\min}(z, r)}^{\mathcal{L}_{\max}(z)} p(\mathcal{L} + \log T_{\text{frac}}(z), r) \times \phi_{\text{true}, \alpha, \mathcal{L}_*}(\mathcal{L} | \phi_*) \frac{dV}{dz d\Omega}(z) r d\mathcal{L} dr dz \quad (11)$$

We now assume that the probability distribution of observing  $N$  galaxies out of an expectation value  $N_k = N_{\alpha, \mathcal{L}_*}(\phi_*)$  obeys Poissonian statistics. The likelihood of

**Table 4.** Ly $\alpha$  Luminosity Function Fitting Parameter Priors

Parameter	Priors
$\alpha$	Uniform on $[-3, 0]$ ; Fixed <sup>a</sup>
$\mathcal{L}_*$	Uniform on $[41.5, 44.0]$
$\log \phi_*$	Uniform on $[-5, -1]$

<sup>a</sup> $\alpha$  is fixed when noted as such.

observing a given  $\phi_*$  is then

$$\begin{aligned} \ln \mathcal{P}_{\phi_* | \alpha, \mathcal{L}_*} &= \ln P_{\text{Poisson}}(N_k; \lambda = N) \\ &= N_k \ln(N) - \ln \Gamma(N_k + 1) - N \end{aligned} \quad (12)$$

Finally, since the overall likelihood of a given Schechter solution is just the product of the  $(\alpha, \mathcal{L}_*)$  and  $\phi_*$  likelihoods, we obtain

$$\ln \mathcal{P}_{\alpha, \mathcal{L}_*, \phi_*} = \ln \mathcal{P}_{\alpha, \mathcal{L}_*} + \ln \mathcal{P}_{\phi_* | \alpha, \mathcal{L}_*} \quad (13)$$

which is the equivalent of Equation 7.

To efficiently perform this calculation, we take advantage of the fact that  $N_{\alpha, \mathcal{L}_*}(\phi_*) \propto \phi_*$ . This allows us to set  $\phi_* = 1$  and calculate the “normalized” number of galaxies over the same grid  $101 \times 101$  grid of  $\alpha$  and  $\mathcal{L}_*$  values used for the computation of  $\mathcal{P}_{\alpha, \mathcal{L}_*, \phi_*}$ . We can then calculate the overall likelihood for any value of  $\alpha$ ,  $\mathcal{L}_*$ , and  $\phi_*$  by performing 2D cubic interpolations over the  $\mathcal{P}_{\alpha, \mathcal{L}_*, \phi_*}$  and  $\phi_* = 1$  grids, multiplying  $N_{\alpha, \mathcal{L}_*}(\phi_* = 1)$  by  $\phi_*$ , and using Equation 12 to calculate the  $\phi_*$  likelihood.

The above algorithm is used to determine the best-fit parameters of the Schechter (1976) function via MCMC chains computed using the `emcee` package (Foreman-Mackey et al. 2013) with 200 walkers (starting positions for random walks) and 5000 steps (number of random walks in each chain). We list the (uniform) priors used for the parameters  $\alpha$ ,  $\mathcal{L}_*$ , and  $\log \phi_*$  in Table 4; these are roughly the smallest possible bounds that could still reproduce any physically viable luminosity function.

## 4. RESULTS

We calculate the Ly $\alpha$  luminosity functions of our LAE candidates in the three ODIN narrow-bands: N419 ( $z \sim 2.4$ ), N501 ( $z \sim 3.1$ ), and N673 ( $z \sim 4.5$ ). As detailed in § 3, we use two methods for computation: 1) a modification of the non-parametric  $V/V_{\text{max}}$  method ( $V_{\text{eff}}$ ) that uses the methodology of Sobral et al. (2018) to estimate the effects of the non-top-hat filter, and 2) a Bayesian MCMC method where we find the most likely

Schechter (1976) parameters by forward modeling the expected shape of the luminosity function. As discussed in § 3.1, the second method is likely to be more accurate, though it is more computationally intensive and is restricted to the provided functional form. We show the results from both methods but focus on those obtained with the MLE-MCMC approach.

#### 4.1. Full-Field Luminosity Functions

Figures 8, 9 and 10 display “triangle plots” for our full sample of  $z \sim 2.4$ , 3.1, and 4.5 LAEs in the extended COSMOS field. The six panels, which take up the bulk of the figures, show the cross-sections for the three Schechter parameters fitted by our MCMC chains. As expected, there is a high degree of correlation among the variables: a common feature of most parameteric fits to  $z \gtrsim 2$  galaxy luminosity functions. But the overall shape of the function is always well defined. This is illustrated in the top right panel of the figures, which displays the results of both the  $V_{\text{eff}}$  method and the  $\sim 3.5\sigma$  range of luminosity functions found by our MCMC analysis. The panels illustrate the excellent agreement between the results of our non-parametric calculations and the fits to the Schechter (1976) functions.

The results of Figures 8 – 10 come with a caveat concerning our error-free treatment of completeness and contamination. Propagating the uncertainties associated with these two effects is algorithmically complex and computationally expensive, although we do employ a simple (but time-intensive) method for approximating the uncertainty in § 3.2 for the N501 data.

Table 5 summarizes our results. Note that although we give the formal uncertainties on the Schechter parameters, the strongly correlated errors of  $\mathcal{L}_*$ ,  $\alpha$ , and  $\phi_*$  (see Figures 8 - 10) are not reflected in the table. However, the integrals of the Schechter function – total number of LAEs and the derived luminosity density of the population – are not subject to these interdependencies. Therefore, their uncertainties are robust and better reflect the evolution of the luminosity functions.

For the remainder of the paper, we focus on the results from the MCMC method given the higher level of rigor in the algorithm and the lower sensitivity to errors in the faint-end completeness.

#### 4.2. Comparisons to the Literature

Figure 11 compares ODIN luminosity functions to the literature, as recorded in the supplemental data section of Sobral et al. (2018) in addition to Herenz et al. (2019). For  $z \sim 2.4$ , we display our fitted luminosity function along with the  $z = 2.2$  results from Konno et al. (2016) (with contamination corrections from Sobral et al. 2017),  $z = 2.4$  data from Matthee et al. (2017),

and  $z \sim 2.5$  measurements from Cassata et al. (2011) and Sobral et al. (2018). At  $z \sim 3.1$ , our luminosity function is compared to the  $z = 3.1$  data of Ouchi et al. (2008) and Matthee et al. (2017) and the  $z = 3.2$  results of Sobral et al. (2018), while for  $z \sim 4.5$  we compare our data to the  $z \sim 4.5$  measurements of Dawson et al. (2007) and Drake et al. (2017), the  $z = 4.6$  data of Sobral et al. (2018), and  $3 < z < 6.7$  (spectroscopic) results of Herenz et al. (2019).

The shaded regions of Figure 11 illustrate the limits of our analysis, i.e., where the corrections for foreground AGN and other contaminants become greater than 50% (or 32% for N673) and where the (effective) completeness decreases to under  $\sim 50\%$ . (For the latter, the exact location is determined by noting where variations in the completeness fractions across the field begin to introduce artifacts into the derived luminosity function.) We can see that at  $\text{Ly}\alpha$  luminosities fainter than  $\log L \sim 43$ , the agreement between our fits and the measurements in the literature is quite reasonable, though the fits tend to be lower than the literature values in the medium and high luminosity regimes for  $z \sim 2.4$  and  $z \sim 3.1$ . At  $z \sim 4.5$ , we have great agreement with the literature.

There are several possible ways to explain the discrepancy between our results for the bright end of the galaxy luminosity function and previous measurements from the literature (for  $z \sim 2.4$  and  $z \sim 3.1$ ). One contributing factor may be our treatment of completeness and contamination. As stated before, the uncertainties in the completeness and purity rate are (generally) not propagated through the analysis, due to algorithmic and computational limitations. However, in Figure 12, we account for these uncertainties in the singular case of the N501 filter and show that they cannot fully explain the discrepancy.

To do this, we created 25 realizations of the effective completeness curve and repeated the analysis described in § 3 in each case, compiling all the posterior samples to determine uncertainties. For the regular part of the completeness curve, we estimate the error as the standard deviation of completeness at different patches at the same radial distance (binned). For the contamination, we assume Poisson-distributed uncertainties. Based on the median solution and  $1 - \sigma$  bounds, we demonstrate that even including uncertainties, we still predict significantly lower values of the luminosity function at  $\log L \gtrsim 43$  than in the literature.

The constraint imposed by a Schechter parameterization (which forces the bright-end of luminosity function to have an exponential cutoff) may partly explain the bright-end discrepancy between our derived luminosity functions and those found by other authors. However,

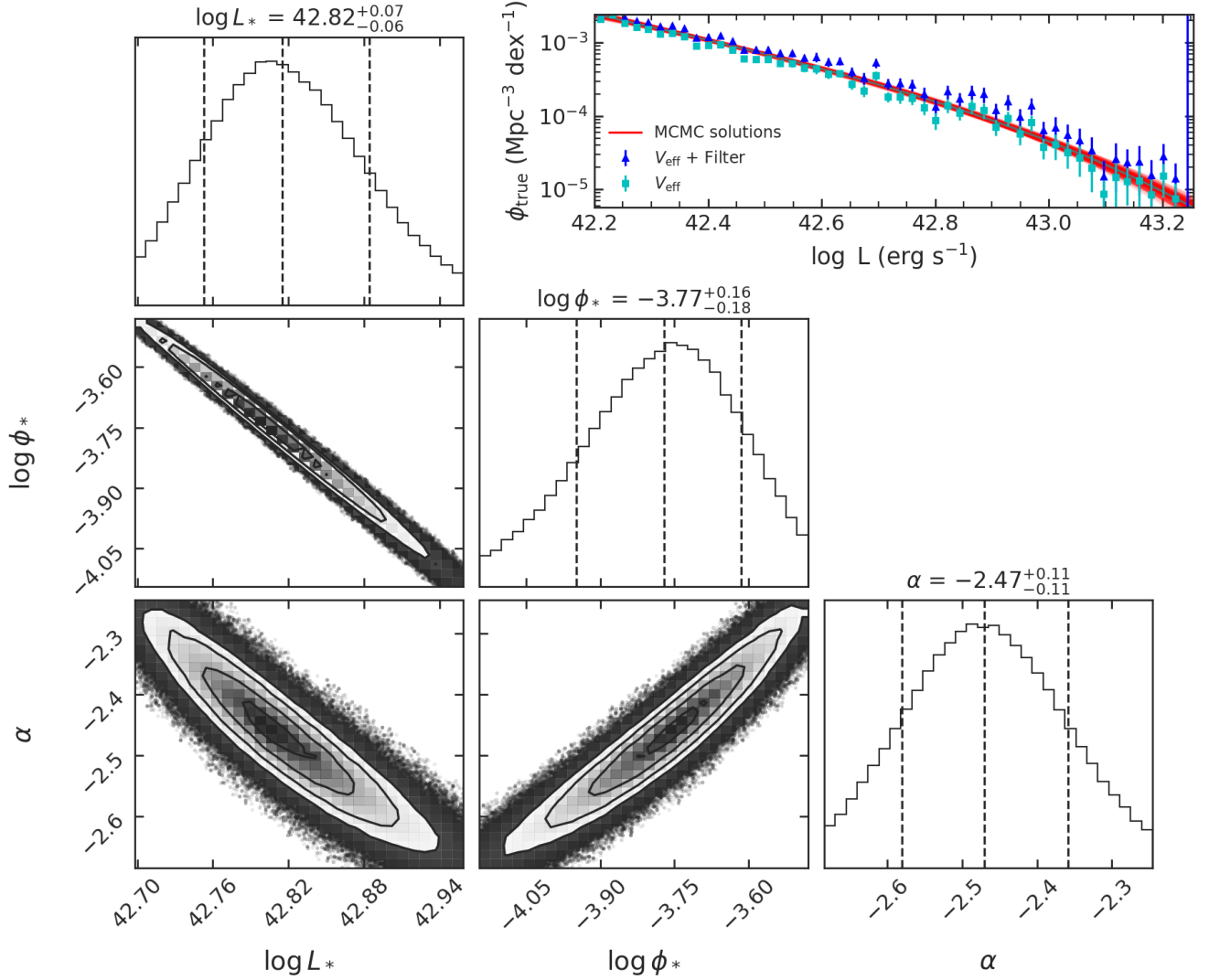


**Figure 8.** Parametric and non-parametric fits to the  $z \sim 2.4$  (N419) Ly $\alpha$  emission-line luminosity function of ODIN LAEs in the extended COSMOS field. The “triangle plot” that takes up most of the figure shows the 1-D and 2-D cross-sections of the parameter space explored by the MCMC chains used to fit the Schechter parameters. The high degree of correlation is expected given the interdependence of the  $L_*$ ,  $\phi_*$  and  $\alpha$ . The red curves in the top right panel show the range (up to  $\sim 3.5\sigma$  away from the median) of luminosity functions given various MCMC solutions. Their small spread demonstrates the stability of the fit, though the errors are underestimated due to the assumption that the completeness and contamination fractions are error-free. The cyan squares show the raw  $V_{\text{eff}}$  results, while the blue triangles include a correction for the uneven filter transmission. We expect the MCMC result to be more accurate, as it is based on a more rigorous mathematical formulation and is less subject to errors in the characterization of faint-end completeness. Nevertheless, we see agreement between the two methods (blue points vs the red curves) is excellent, albeit with significant non-smooth variations in the  $V_{\text{eff}}$  method.

we suspect that the principal reason for our systematically lower numbers at the bright end is our new, more rigorous treatment of contamination. The  $\sim 2800$  DESI spectra obtained over the full range N419 and N501 Ly $\alpha$  luminosities have allowed us to trace the fraction of interlopers as a function of brightness, and remove a source of contamination that is difficult to identify in most LAE surveys. Had we not done this, our luminos-

ity function would more closely follow those of previous measurements.

Because the Schechter parameters  $\mathcal{L}_*$ ,  $\alpha$ , and  $\phi_*$  are not orthogonal, fits using the function generally result in strong degeneracies between the parameters. Different combinations of variables can yield similar solutions in the region where data exist, but make very different predictions for the faint end slope, where the data are becoming incomplete. In this case of our ODIN data,

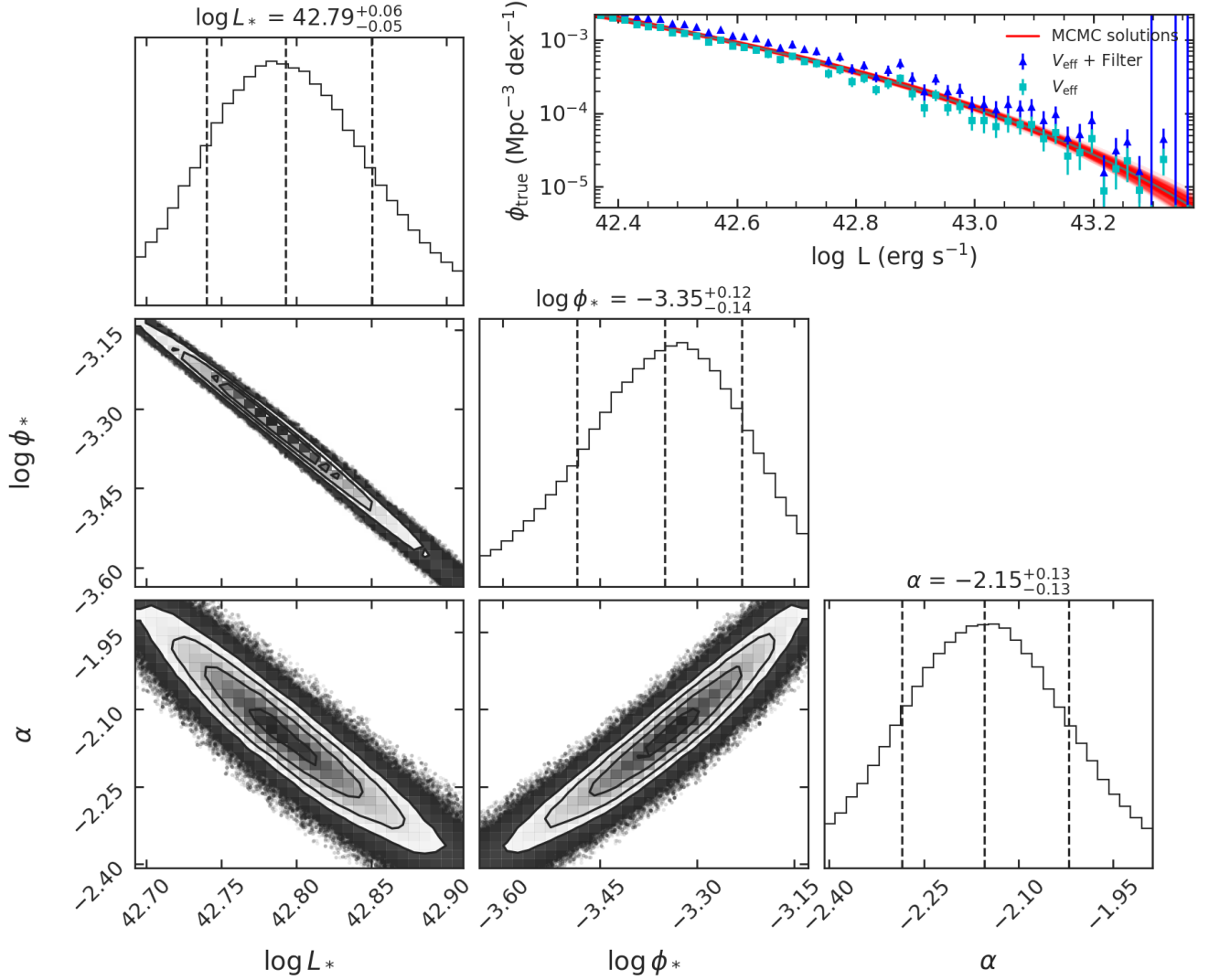


**Figure 9.** Parametric and non-parametric fits to the  $z \sim 3.1$  (N501) Ly $\alpha$  emission-line luminosity function of LAEs. The panels are the same as in Figure 8. Once again, we find excellent agreement between the two methods.

**Table 5.** Full Field Ly $\alpha$  Luminosity Functions

Band	$z$	LAEs	$\geq 50\% C^a$	$\mathcal{L}_*$	$\alpha$	$\log \phi_*$	$\log \int_{42.5}^{\infty} \phi(\mathcal{L}) d\mathcal{L}$ (Mpc $^{-3}$ )	$\log \int_{42.5}^{\infty} 10^{\mathcal{L}} \phi(\mathcal{L}) d\mathcal{L}$ ( $L_{\odot}$ Mpc $^{-3}$ )
N419	2.4	6100	3310	$42.82^{+0.07}_{-0.06}$	$-2.47^{+0.11}_{-0.11}$	$-3.77^{+0.16}_{-0.18}$	$-3.87^{+0.01}_{-0.01}$	$5.25^{+0.01}_{-0.01}$
N501	3.1	5782	3413	$42.79^{+0.06}_{-0.05}$	$-2.16^{+0.13}_{-0.13}$	$-3.35^{+0.12}_{-0.14}$	$-3.53^{+0.01}_{-0.01}$	$5.61^{+0.01}_{-0.01}$
N673	4.5	4101	2684	$43.12^{+0.06}_{-0.06}$	$-2.01^{+0.12}_{-0.11}$	$-3.78^{+0.12}_{-0.14}$	$-3.44^{+0.01}_{-0.01}$	$5.79^{+0.01}_{-0.01}$

<sup>a</sup>Number of LAEs actually included in the analysis (effective completeness between  $\sim 0.5$  and 2)

our best-fit Schechter solutions favor steep  $\alpha$  values, especially for  $z \sim 2.4$ , where faint end slope approaches  $\alpha \sim -2.5$ . We suggest caution when considering the

luminosity function values in the shaded region below  $\sim 50\%$  completeness.

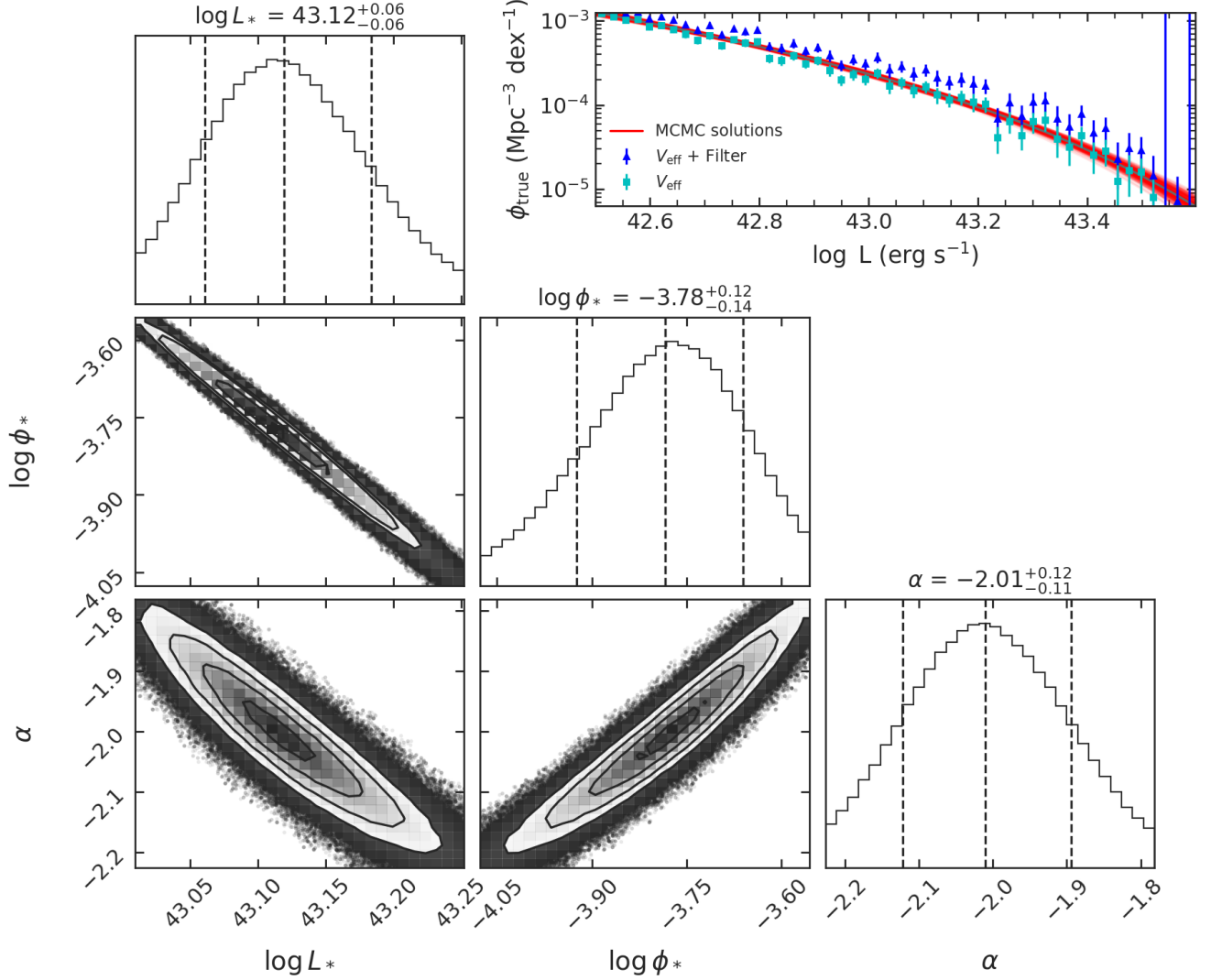


**Figure 10.** Parametric and non-parametric fits to the  $z \sim 4.5$  (N673) Ly $\alpha$  emission-line luminosity function of LAEs. The panels are the same as in Figure 8. Relative to N419 and N501, these data probe higher luminosities and are more uncertain at the bright end, due to our poorer understanding of foreground contamination. Nevertheless, the luminosity function displays the same general behavior as those of the N419 and N501 LAEs. .

An important point to note is that most works are unable to place strong constraints on  $\alpha$ , and thus fix the faint-end slope to some reasonable value (see Ouchi et al. 2020), which is always shallower than the values obtained in this analysis. As a result there is little data available for a true comparison.

While Figure 11 shows our results at all three redshifts, Figure 13 highlights the cosmic evolution of the LAE luminosity function by putting the three curves in a single panel. The data suggest that the faint-end slope of the luminosity function flattens and the total number and luminosity density of LAEs (down to  $\log L = 42.5$ ) increases with redshift. Unfortunately, it is difficult to claim that these trends are statistically significant due

to the underestimated and highly correlated uncertainties in the parameters. The increase in the luminosity density between  $z \sim 2.4$  and  $z \sim 3.1$  is consistent with the  $z < 3$  trends seen in the literature (Ouchi et al. 2020, and references therein). The increase from  $z \sim 3.1$  to  $z \sim 4.5$  is smaller, in line but not fully consistent with the lack of evolution seen at  $3 < z < 6$ .

### 4.3. Environmental Trends

One of the primary goals of ODIN is to identify the protoclusters, filaments, and voids of the  $z > 2$  universe; quantify each LAE’s environment; and examine galaxy evolution versus environment. The  $z \sim 2.4, 3.1$  and  $4.5$  large scale structure present in COSMOS has already

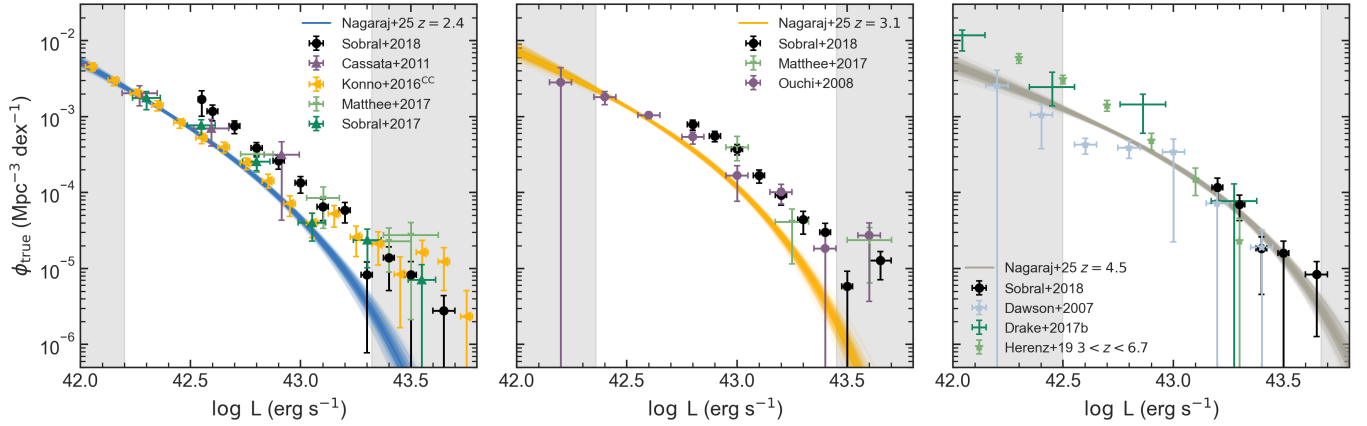


**Figure 11.** The ODIN LAE Ly $\alpha$  luminosity functions at redshifts  $z \sim 2.4$  (left),  $z \sim 3.1$  (middle), and  $z \sim 4.5$  (right) compared to results in the literature. The light blue curve shows the range (up to  $\sim 3.5\sigma$  from the median) of our MCMC solution; the gray-shaded regions show where the corrections are greater than a factor of  $\sim 2$ , either due to photometric incompleteness or foreground contamination. Our results agree with the literature at  $\log L \lesssim 43$  but tend to be lower in value at high luminosities. See §3.2 for a more detailed discussion.

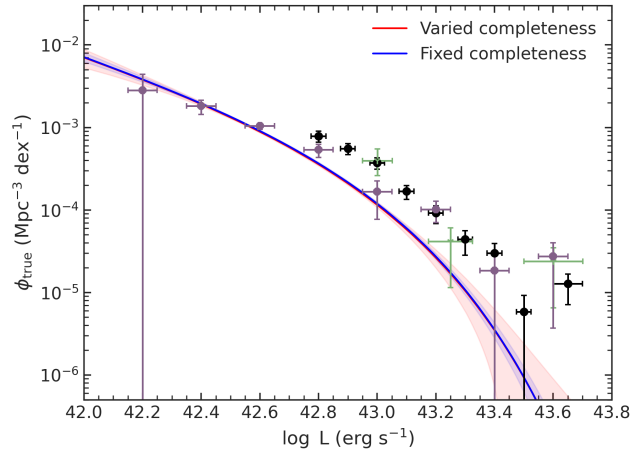


**Figure 12.** Luminosity function solutions and  $1-\sigma$  bounds in the cases where we account for uncertainties in the effective completeness (red) and do not do so (blue). While it is clear that the uncertainties are much larger in the former case, especially at the bright end, they are not enough to explain the discrepancy between our results and the literature (various points, with the same colors and markers as in the middle panel of Figure 11).

been quantified using both Gaussian kernel smoothed density maps and Voronoi tessellation (Ramakrishnan et al. 2023, 2024) and a number of extremely rich protoclusters have been identified. Here we take advantage of these measurements and examine the epochs’ Ly $\alpha$  luminosity functions as a function of environment.

For our analysis, we use the identification of protoclusters computed by Ramakrishnan et al. (2023, 2024), based on Voronoi tessellation (e.g., Darvish et al. 2015) of the LAE distribution. In the analysis of Ramakrishnan et al. (2024), the local surface density is given by the

inverse of the Voronoi cell size; the resulting surface density map is then normalized to one and convolved with a 5 cMpc Gaussian kernel. These density estimates are imperfect: the FWHMs of the N419, N501, and N673 filters correspond to co-moving line-of-sight widths of 75, 60, and 50 cMpc, respectively, while the typical size of a  $z \sim 3$  protocluster is  $\sim 10$  cMpc (e.g., Chiang et al.

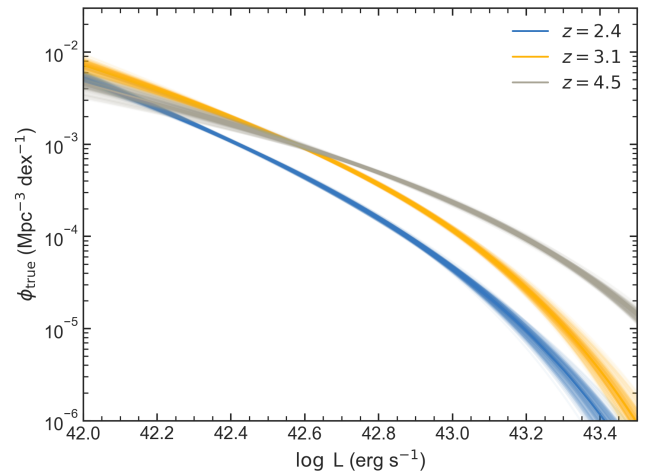


**Figure 13.** Schechter fits to the ODIN data showing cosmic evolution of the Ly $\alpha$  luminosity function. The increase in the total number of galaxies with redshift is consistent with the known strong evolution out to  $z \sim 3$ . The evolution does seem to continue to  $z \sim 4.5$ , less consistent with the minimal LAE evolution between  $3 < z < 6$  (Ouchi et al. 2020). Nevertheless, the bulk of these differences are at the bright end, where the number of spectra available for understanding contamination is still low for  $z \sim 4.5$ . There is some evidence for a gradual flattening of the faint-end slope with redshift, but larger and/or deeper samples are needed to confirm this feature.

2013; Muldrew et al. 2015). As a result, projection effects dilute the overdensity measures. Nevertheless, the analysis of simulated data from IllustrisTNG (Pillepich et al. 2018; Nelson et al. 2019) shows that most proto-clusters will be found by the ODIN algorithms and that the cosmic web in the vicinity of proto-clusters can be recovered quite accurately (Ramakrishnan et al. 2024).

Before we can derive the environmental dependence of the luminosity function, we must revisit the issue of foreground contamination and its effect on the measurements. The distribution of foreground interlopers, such as mis-identified AGN and [O II] emitters, should be completely uncorrelated with that of correct-redshift LAEs. Consequently, the ratio of interlopers to LAEs should change with environment: the denser the environment, the smaller the fraction of foreground contaminants. Since our analysis algorithms treat these interlopers as ‘overcompleteness’ (see § 2.2), the use of a single multiplicative correction factor for all environments would introduce a systematic error into the results. To avoid this problem, we modify the completeness curves of Figure 4 by dividing the expected number of foreground contaminants defined in Section 2.2 by the ratio of the given environment’s median LAE density to the overall LAE density in the field.

We note, however, that some of the contaminants in our LAE sample are AGN exhibiting broad Ly $\alpha$  at the correct redshift. Unlike the foreground contaminants, these objects will be correlated with LAE environment, likely in some complex fashion. For purposes of our luminosity function measurement, we assume a simple one-to-one correspondence, with the density of Ly $\alpha$ -detected AGN scaling exactly with the density of LAEs. These objects are not modified in the calculation of the purity fraction vs. environments. Given the small number of such sources, the exact relationship between AGN and LAE clustering makes little difference to the overall result.

Using the modified effective completeness curves, we examine the behavior of the LAE Ly $\alpha$  luminosity functions versus environment. At each redshift, we divide our LAE sample into those in proto-clusters and those in the field and compute the luminosity functions in each environment. To estimate the effective areas encompassed by the proto-clusters and the field,

1. we approximate the (relative) area occupied by each individual source as the inverse of its local surface density.
2. we sum these ‘‘areas’’ for every object with a local surface density ranked between the 5th and 95th percentile for either proto-clusters or field. We do

not include extremes to avoid densities near zero, which can lead to extremely large and biased sums.

3. we multiply the entire survey area by the ratio of the total area occupied by galaxies in the environment to the total area occupied by all galaxies. This gives us the effective survey area for the different sets of LAEs.

As mentioned earlier, proto-clusters occupy a much smaller redshift interval than that recorded by our narrow-band filters’ FWHM. As a result, our proto-clusters are diluted by field galaxies lying within the angular region of the proto-clusters but physically foreground or background to the structure. Without follow-up spectroscopy, our analysis cannot account for this effect. Thus, as discussed in Andrews et al. (2024), the differences between our proto-cluster and field luminosity functions are likely muted compared to reality.

Figures 14 and 15, along with Table 6, show how the behavior of the Ly $\alpha$  luminosity function changes with environment and cosmic time. Naturally, the normalizations of the curves are different: the number density of galaxies in proto-clusters is  $\sim 0.5$  dex higher than that of the field environment (see the last panel of Figure 15). For comparison, the simulations of Andrews et al. (2024) find a shift of  $\sim 1$  dex for similar redshifts, suggesting that our proto-cluster data may be diluted by field galaxies by a factor of  $\sim 3$ .

A second and more interesting feature is a slight difference in the shapes of the luminosity functions: the proto-cluster luminosity functions seem to have a ‘‘bulge’’ at medium luminosities, with shallower faint-end slopes and more rapid exponential declines at high luminosities. This is most visible in Figure 14. In terms of Schechter parameters (Figure 15), this can be seen as a shallower faint-end slope  $\alpha$  (at all three redshifts). If true, the data would suggest a tendency for the suppression of both very low- and very high-luminosity LAEs in dense environments. Alternatively, it could be that proto-clusters tend to enhance medium-luminosity LAEs more than fainter or brighter LAEs. In general, the results would imply that, even at  $z \sim 3$ , environment is playing a role in regulating the creation of Ly $\alpha$  photons and/or their escape. However, these trends are certainly not statistically significant, requiring larger proto-cluster samples for a more definitive result.

The shallower faint-end slopes in proto-clusters are in agreement with the simulation-based results of Andrews et al. (2024), including the finding that the difference between the Ly $\alpha$  luminosity function in the proto-clusters vs. the field is not very significant. Andrews et al. (2024) attribute the shallower slopes, especially for the

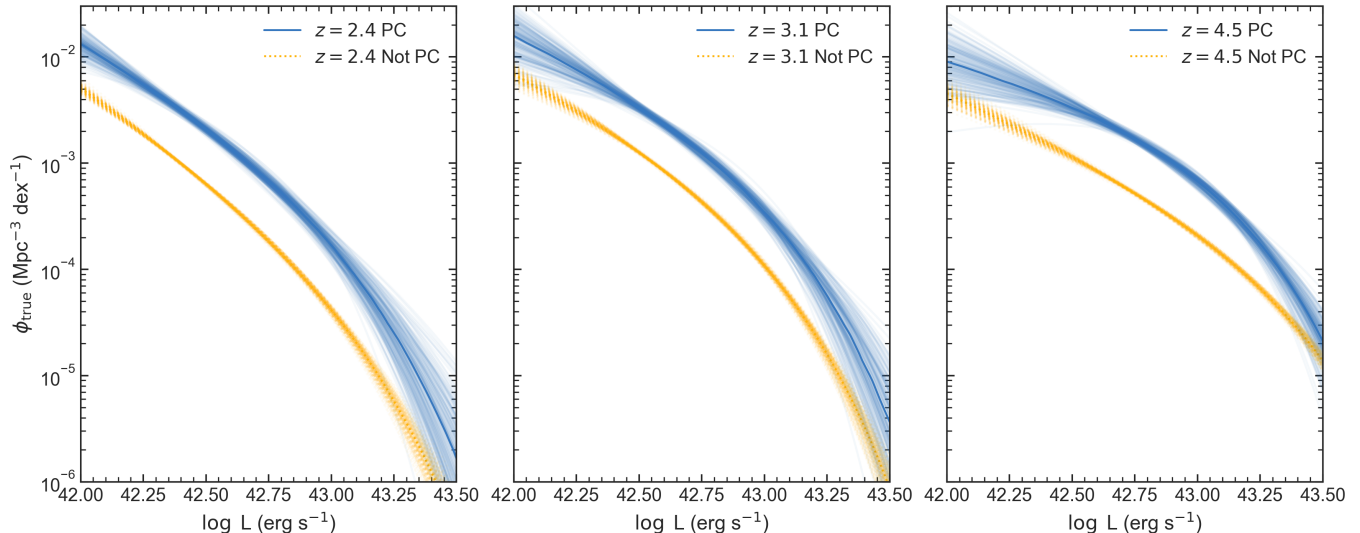


**Figure 14.** Comparison of the Schechter fits for the LAE luminosity functions in protoclusters (blue) and the field (yellow) at each of the three ODIN redshifts (left:  $z \sim 2.4$ , middle:  $z \sim 3.1$ , right:  $z \sim 4.5$ ). The much greater ( $\sim 3.5\sigma$ ) range of MCMC solutions for the protocluster luminosity functions reflects the relatively small number of LAEs found within these systems. While the protocluster luminosity functions are universally elevated compared to the field, there also some intriguing differences in shape: either a) both very faint and very bright protocluster LAEs appear to be suppressed relative to the field or b) medium-bright LAEs are particularly enhanced. If borne out by further data, this would suggest that environmental processing has begun, even in these non-relaxed systems.

UV luminosity function, to differences in galaxy formation pathways. Our lack of a clear trend with  $L_*$  is consistent with Andrews et al. (2024) but in disagreement with the result of Dey et al. (2016), who found lower LAE luminosities at larger distances from the center of a  $z \sim 3.8$  protocluster. (Dey et al. (2016) attributed the feature to enhanced star formation and/or AGN activity.) Meanwhile, Andrews et al. (2024) do find a bright excess in the UV luminosity function. The implication of a possible suppression of high-luminosity LAEs in our work is consistent with the simulations of Andrews et al. (2024).

Unfortunately, any interpretation of our results with regard to simulations is premature. As illustrated in Figures 8 – 10,  $L_*$  and  $\alpha$  are strongly correlated so any mis-estimation in the direction of a shallower slope also results in an underestimate of  $L_*$ . In fact, a comparison of the  $\log L_* - \alpha$  likelihood contours shown in Figure 16 demonstrates that there is a modest amount of overlap in the two populations’ posterior distribution functions. A much larger set of protoclusters will be needed to determine whether there is true difference in the luminosity function shapes. The full ODIN survey will provide such a sample.

## 5. CONCLUSION

We have used ODIN narrow-band data in the  $\sim 9$  deg<sup>2</sup> Extended COSMOS field to measure LAE Ly $\alpha$  luminosity functions in and out of protoclusters at three

different redshifts. Our sample consists of 6100 LAE candidates at  $z \sim 2.4$ , 5782 at  $z \sim 3.1$ , and 4101 at  $z \sim 4.5$  selected via the techniques described by Firestone et al. (2024). The purity of this sample has been measured via DESI spectroscopy of  $\sim 2800$  ODIN LAEs satisfying these same selection criteria. These data show that overall, the fraction of interlopers is low: less than 10% at  $z \sim 2.4$  and 3.1, and  $\lesssim 20\%$  at  $z \sim 4.5$ . However, our analysis also shows that this contamination rate is a strong function of luminosity, mainly because of the inclusion of foreground AGN at bright luminosities.

We compute the luminosity function by modifying existing algorithms to handle large numbers of LAEs and the wide-field aspects of the ODIN survey. One unique feature of our analysis is our treatment of the contamination versus luminosity relation as “over-completeness” in the LAE number counts; this formalism unites the concepts of photometric incompleteness and sample purity in a single quantity and allows us to more rigorously account for the issue of AGN contamination at the bright end. To ensure that these corrections do not introduce spurious artifacts into our results, we restrict our analysis to the LAE luminosities where the fraction of contaminants is less than 50% and the photometric completeness is greater than  $\sim 50\%$ . This leaves us with a sample of 3310 LAEs at  $z \sim 2.4$ , 3413 LAEs at  $z \sim 3.1$ , and 2575 objects at  $z \sim 4.5$ .

We outline both a parametric and non-parametric method of deriving our LAE luminosity functions. For

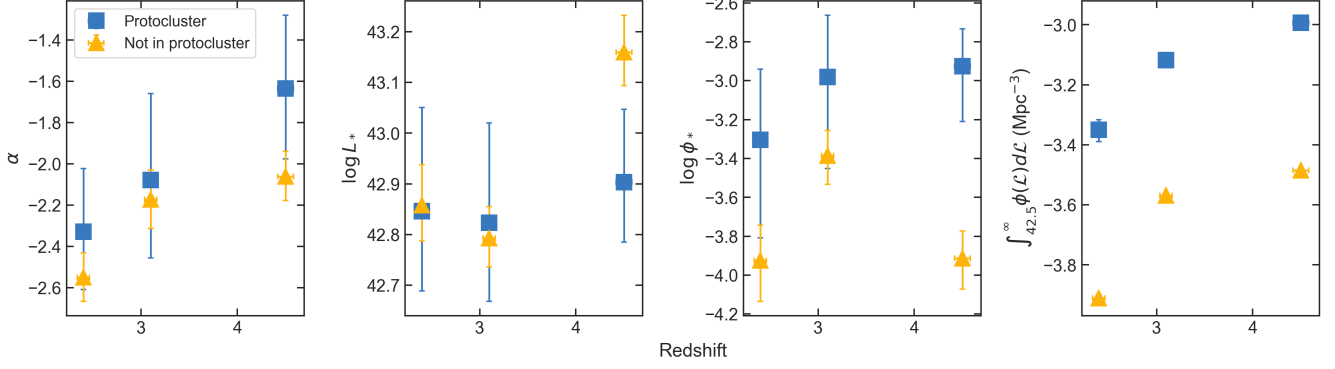


**Figure 15.** The evolution of the Schechter parameters in and out of protoclusters, as found from the ODIN data of the extended COSMOS field. In the first three panels, we show the values of the faint-end slope, the characteristic luminosity, and the normalization parameter, with the protocluster fits in blue and the field results in yellow. In the last panel, we show the integrated number density of LAEs. Unsurprisingly, the LAE number densities within protoclusters are  $\sim 0.5$  dex higher than in the field. The slight trend for  $\alpha$  to be flatter in protoclusters causes most of the differences in shape seen in Figure 14.

**Table 6.** Environmental Impacts on the Ly $\alpha$  Luminosity Function

$z$	PC?	Number of LAEs <sup>a</sup>	Field Fraction <sup>b</sup>	$L_*$	$\alpha$	$\log \phi_*$	$\log \int_{42.5}^{\infty} \phi(L)dL$ (Mpc <sup>-3</sup> )	$\log \int_{42.5}^{\infty} 10^L \phi(L)dL$ ( $L_{\odot}$ Mpc <sup>-3</sup> )
2.4	Y	410	0.04	$42.85^{+0.20}_{-0.16}$	$-2.33^{+0.31}_{-0.28}$	$-3.30^{+0.36}_{-0.50}$	$-3.35^{+0.03}_{-0.04}$	$5.79^{+0.03}_{-0.04}$
2.4	N	2904	0.96	$42.86^{+0.08}_{-0.07}$	$-2.55^{+0.12}_{-0.12}$	$-3.92^{+0.18}_{-0.21}$	$-3.91^{+0.01}_{-0.01}$	$5.21^{+0.01}_{-0.01}$
3.1	Y	373	0.04	$42.82^{+0.20}_{-0.15}$	$-2.08^{+0.42}_{-0.38}$	$-2.98^{+0.32}_{-0.47}$	$-3.12^{+0.02}_{-0.03}$	$6.03^{+0.03}_{-0.03}$
3.1	N	3040	0.96	$42.79^{+0.06}_{-0.06}$	$-2.17^{+0.14}_{-0.14}$	$-3.38^{+0.13}_{-0.15}$	$-3.57^{+0.01}_{-0.01}$	$5.57^{+0.01}_{-0.01}$
4.5	Y	417	0.06	$42.90^{+0.14}_{-0.12}$	$-1.63^{+0.35}_{-0.34}$	$-2.93^{+0.19}_{-0.28}$	$-2.99^{+0.02}_{-0.02}$	$6.22^{+0.03}_{-0.02}$
4.5	N	2267	0.94	$43.16^{+0.07}_{-0.07}$	$-2.06^{+0.12}_{-0.12}$	$-3.91^{+0.14}_{-0.16}$	$-3.49^{+0.01}_{-0.01}$	$5.74^{+0.01}_{-0.01}$

<sup>a</sup>Number only includes those LAEs included in the calculation.

<sup>b</sup>Fraction of the Extended COSMOS area within the environment (see §4.3).

the latter, we modify the well-known  $1/V_{\max}$  method to include differential volume effects caused by having a non-top-hat filter. This accounts for the fact that LAEs with faint Ly $\alpha$  emission will only be detected if their redshift places the line near the peak of the filter’s transmission curve, whereas brighter LAEs will be identifiable over a much wider redshift range. We use the Monte Carlo experiment outlined by Sobral et al. (2018) to correct for this effect as well as the systematic underestimation of luminosities arising from the same issue.

For the parametric method, we fit for the traditional Schechter parameters using a maximum likelihood analysis similar to that described in Gronwall et al. (2007) and Nagaraj et al. (2023). To increase computational efficiency, we separate the likelihood calculations for the shape parameters ( $\alpha$ ,  $L_*$ ) from the function’s overall normalization ( $\phi_*$ ). All of the effects of completeness

and the non-top-hat filter curve are included with mathematical rigor.

Our full-field luminosity functions derived by the two methods are in excellent agreement. Our results also agree with the epochs’ luminosity functions found in the literature at  $\log L \lesssim 42.5$ . Our results tend to be lower than the literature values at higher luminosities, though we suspect that is related to our choice to use DESI spectroscopy to statistically remove contaminating objects from the analysis.

Our LAE luminosity functions increase (in integrated number density) with increasing redshift, though very little between  $z \sim 3.1$  and  $z \sim 4.5$ ; this is consistent with known trends (Ouchi et al. 2020, and references therein). We also find a flattening of faint-end slopes with increasing redshift.

One of the main goals of the ODIN survey is to use LAEs as tracers of  $z \sim 3$  large-scale structure and exam-

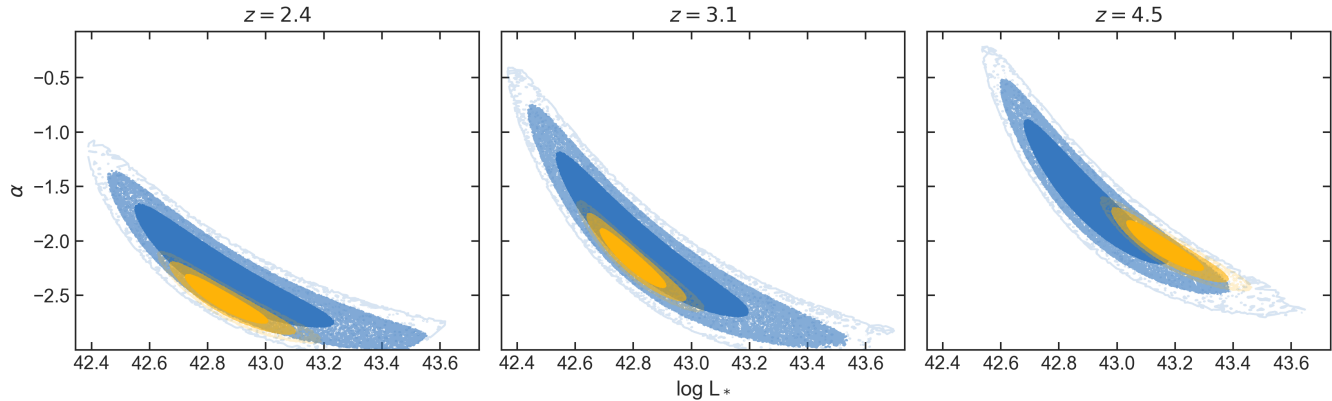


**Figure 16.** Comparison of the likelihood contours of  $\alpha$  and  $\log L_*$  for LAEs in  $z = 2.4, 3.1,$  and  $4.5$  protoclusters (blue) and the field (yellow) as derived via MCMC method. The Figure show 1-, 2- and 3- $\sigma$  contour levels in increasing transparency of the colors. The two sets of contours overlap in all three bands, meaning that at this time, we cannot confidently draw any conclusions about the effect on environment on the LAE luminosity function.

ine the effects of environment on galaxy evolution. To this end, Ramakrishnan et al. (2023, 2024) have quantified the LAE surface density throughout the Extended COSMOS field and have identified several protoclusters at each of the three ODIN redshifts. That has allowed us to compare LAE luminosity functions in and out of protoclusters and test for differences. We find some evidence that the LAE luminosity function in protoclusters is either suppressed at both very bright and very faint luminosities or enhanced at medium luminosities compared to the field. However, at present, the sample of ODIN protoclusters is not sufficient for a definitive result.

This work is the first analysis of LAE luminosity functions based on ODIN photometry; its main purpose is to develop the algorithms necessary to examine the effect of environment on the shape of LAE Ly $\alpha$  luminosity functions from  $z \sim 2.4$  to  $z \sim 4.5$ . The LAEs in the COSMOS field alone are insufficient for this purpose. In contrast, the final ODIN footprint will contain an order of magnitude more data than that used here and the final number of rich protoclusters will number in the hundreds. This will allow greater insight into the effect environment on the early history of galaxy formation.

#### ACKNOWLEDGMENTS

R.C. and C.G. acknowledge support from the National Science Foundation under grant AST-2408358. The Institute for Gravitation and the Cosmos is supported by the Eberly College of Science and the Office of the Senior Vice President for Research at the Pennsylvania State University. KSL and VR acknowledge financial support

from the National Science Foundation under Grant Nos. AST-2206705 and AST-2408359.

This material is based upon work supported by the U.S. Department of Energy (DOE), Office of Science, Office of High-Energy Physics, under Contract No. DE-AC02-05CH11231, and by the National Energy Research Scientific Computing Center, a DOE Office of Science User Facility under the same contract. Additional support for DESI was provided by the U.S. National Science Foundation (NSF), Division of Astronomical Sciences under Contract No. AST-0950945 to the NSF's National Optical-Infrared Astronomy Research Laboratory; the Science and Technology Facilities Council of the United Kingdom; the Gordon and Betty Moore Foundation; the Heising-Simons Foundation; the French Alternative Energies and Atomic Energy Commission (CEA); the National Council of Humanities, Science and Technology of Mexico (CONACYT); the Ministry of Science, Innovation and Universities of Spain (MICIU/AEI/10.13039/501100011033), and by the DESI Member Institutions: <https://www.desi.lbl.gov/collaborating-institutions>. Any opinions, findings, and conclusions or recommendations expressed in this material are those of the author(s) and do not necessarily reflect the views of the U. S. National Science Foundation, the U. S. Department of Energy, or any of the listed funding agencies.

The authors are honored to be permitted to conduct scientific research on I'oligam Du'ag (Kitt Peak), a mountain with particular significance to the Tohono O'odham Nation.

*Software:* NumPy (Harris et al. 2020), AstroPy (Astropy Collaboration et al. 2013, 2018, 2022), SciPy (Jones et al. 2001–; Virtanen et al. 2020), Matplotlib (Hunter

2007), emcee (Foreman-Mackey et al. 2013), Corner (Foreman-Mackey 2016), Seaborn (Waskom 2021)

## REFERENCES

- Adame, A. G., Aguilar, J., Ahlen, S., et al. 2025a, JCAP, 2025, 124  
 —. 2025b, JCAP, 2025, 021  
 —. 2025c, JCAP, 2025, 012  
 Aihara, H., Arimoto, N., Armstrong, R., et al. 2018, PASJ, 70, S4  
 Aihara, H., AlSayyad, Y., Ando, M., et al. 2019, PASJ, 71, 114  
 Andrews, M., Artale, M. C., Kumar, A., et al. 2024, arXiv e-prints, arXiv:2410.08412  
 Astropy Collaboration, Robitaille, T. P., Tollerud, E. J., et al. 2013, A&A, 558, A33  
 Astropy Collaboration, Price-Whelan, A. M., Sipőcz, B. M., et al. 2018, AJ, 156, 123  
 Astropy Collaboration, Price-Whelan, A. M., Lim, P. L., et al. 2022, ApJ, 935, 167  
 Avni, Y., & Bahcall, J. N. 1980, ApJ, 235, 694  
 Bennett, C. L., Larson, D., Weiland, J. L., et al. 2013, ApJS, 208, 20  
 Bertin, E., & Arnouts, S. 1996, A&AS, 117, 393  
 Caruana, J., Wisotzki, L., Herenz, E. C., et al. 2018, MNRAS, 473, 30  
 Cassata, P., Le Fèvre, O., Garilli, B., et al. 2011, A&A, 525, A143  
 Chiang, Y.-K., Overzier, R., & Gebhardt, K. 2013, ApJ, 779, 127  
 Ciardullo, R., Gronwall, C., Adams, J. J., et al. 2013, ApJ, 769, 83  
 Darvish, B., Mobasher, B., Sobral, D., Scoville, N., & Aragon-Calvo, M. 2015, ApJ, 805, 121  
 Dawson, S., Rhoads, J. E., Malhotra, S., et al. 2007, ApJ, 671, 1227  
 DESI Collaboration, Aghamousa, A., Aguilar, J., et al. 2016a, arXiv e-prints, arXiv:1611.00036  
 —. 2016b, arXiv e-prints, arXiv:1611.00037  
 DESI Collaboration, Abareshi, B., Aguilar, J., et al. 2022, AJ, 164, 207  
 DESI Collaboration, Adame, A. G., Aguilar, J., et al. 2024a, AJ, 167, 62  
 —. 2024b, AJ, 168, 58  
 —. 2024c, arXiv e-prints, arXiv:2411.12020  
 —. 2024d, arXiv e-prints, arXiv:2411.12021  
 —. 2024e, arXiv e-prints, arXiv:2411.12022  
 DESI Collaboration, Abdul-Karim, M., Adame, A. G., et al. 2025a, arXiv e-prints, arXiv:2503.14745  
 DESI Collaboration, Abdul-Karim, M., Aguilar, J., et al. 2025b, arXiv e-prints, arXiv:2503.14738  
 Dey, A., Lee, K.-S., Reddy, N., et al. 2016, ApJ, 823, 11  
 Dey, A., Schlegel, D. J., Lang, D., et al. 2019, AJ, 157, 168  
 Drake, A. B., Garel, T., Wisotzki, L., et al. 2017, A&A, 608, A6  
 Eather, R. H., & Reasoner, D. L. 1969, ApOpt, 8, 227  
 Eddington, A. S. 1913, MNRAS, 73, 359  
 Eddington, A. S., S. 1940, MNRAS, 100, 354  
 Firestone, N. M., Gawiser, E., Ramakrishnan, V., et al. 2024, ApJ, 974, 217  
 Foreman-Mackey, D. 2016, Journal of Open Source Software, 1, 24  
 Foreman-Mackey, D., Hogg, D. W., Lang, D., & Goodman, J. 2013, PASP, 125, 306  
 Gawiser, E., Francke, H., Lai, K., et al. 2007, ApJ, 671, 278  
 Gronwall, C., Ciardullo, R., Hickey, T., et al. 2007, ApJ, 667, 79  
 Guaita, L., Acquaviva, V., Padilla, N., et al. 2011, ApJ, 733, 114  
 Guy, J., Bailey, S., Kremin, A., et al. 2023, AJ, 165, 144  
 Harris, C. R., Millman, K. J., van der Walt, S. J., et al. 2020, Nature, 585, 357  
 Herenz, E. C., Wisotzki, L., Saust, R., et al. 2019, A&A, 621, A107  
 Herrero Alonso, Y., Krumpke, M., Wisotzki, L., et al. 2021, A&A, 653, A136  
 Hill, G. J., Lee, H., MacQueen, P. J., et al. 2021, AJ, 162, 298  
 Huchra, J., & Sargent, W. L. W. 1973, ApJ, 186, 433  
 Hunter, J. D. 2007, Computing in Science & Engineering, 9, 90  
 Im, S. H., Hwang, H. S., Park, J., et al. 2024, ApJ, 972, 196  
 Jacoby, G. H., Quigley, R. J., & Africano, J. L. 1987, PASP, 99, 672  
 Jones, E., Oliphant, T., Peterson, P., et al. 2001–, SciPy: Open source scientific tools for Python  
 Konno, A., Ouchi, M., Nakajima, K., et al. 2016, ApJ, 823, 20  
 Kraljic, K., Arnouts, S., Pichon, C., et al. 2018, MNRAS, 474, 547  
 Lee, K.-S., Dey, A., Hong, S., et al. 2014, ApJ, 796, 126  
 Lee, K.-S., Gawiser, E., Park, C., et al. 2024, ApJ, 962, 36  
 Levi, M., Bebek, C., Beers, T., et al. 2013, arXiv e-prints, arXiv:1308.0847  
 Lynden-Bell, D. 1971, MNRAS, 155, 95  
 Ma, K., Zhang, H., Cai, Z., et al. 2024, ApJ, 961, 102  
 Matthee, J., Sobral, D., Best, P., et al. 2017, MNRAS, 471, 629  
 McCarron, A. P., Finkelstein, S. L., Chavez Ortiz, O. A., et al. 2022, ApJ, 936, 131  
 Mehta, V., Scarlata, C., Colbert, J. W., et al. 2015, ApJ, 811, 141  
 Muldrew, S. I., Hatch, N. A., & Cooke, E. A. 2015, MNRAS, 452, 2528  
 Nagaraj, G., Ciardullo, R., Bowman, W. P., Lawson, A., & Gronwall, C. 2023, ApJ, 943, 5  
 Nelson, D., Springel, V., Pillepich, A., et al. 2019, Computational Astrophysics and Cosmology, 6, 2  
 O’Kane, C. J., Kuchner, U., Gray, M. E., & Aragón-Salamanca, A. 2024, MNRAS, 534, 1682  
 Oke, J. B. 1974, ApJS, 27, 21  
 Ouchi, M., Ono, Y., & Shibuya, T. 2020, ARA&A, 58, 617  
 Ouchi, M., Shimasaku, K., Akiyama, M., et al. 2008, ApJS, 176, 301  
 Ouchi, M., Harikane, Y., Shibuya, T., et al. 2018, PASJ, 70, S13  
 Pillepich, A., Springel, V., Nelson, D., et al. 2018, MNRAS, 473, 4077  
 Poppett, C., Tyas, L., Aguilar, J., et al. 2024, AJ, 168, 245  
 Ramakrishnan, V., Moon, B., Im, S. H., et al. 2023, ApJ, 951, 119  
 Ramakrishnan, V., Lee, K.-S., Artale, M. C., et al. 2024, arXiv e-prints, arXiv:2406.08645  
 Santos, S., Sobral, D., Butterworth, J., et al. 2021, MNRAS, 505, 1117  
 Schechter, P. 1976, ApJ, 203, 297  
 Schlafly, E. F., Kirkby, D., Schlegel, D. J., et al. 2023, AJ, 166, 259  
 Schmidt, M. 1968, ApJ, 151, 393  
 —. 1970, ApJ, 162, 371  
 Shimasaku, K., Kashikawa, N., Doi, M., et al. 2006, PASJ, 58, 313  
 Silber, J. H., Fagrellius, P., Fanning, K., et al. 2023, AJ, 165, 9  
 Sobral, D., Santos, S., Matthee, J., et al. 2018, MNRAS, 476, 4725  
 Sobral, D., Matthee, J., Best, P., et al. 2017, MNRAS, 466, 1242  
 Valdes, F., Gruendl, R., & DES Project. 2014, in Astronomical Society of the Pacific Conference Series, Vol. 485, Astronomical Data Analysis Software and Systems XXIII, ed. N. Manset & P. Forshay, 379

Virtanen, P., Gommers, R., Oliphant, T. E., et al. 2020, Nature Methods, 17, 261

Waskom, M. L. 2021, Journal of Open Source Software, 6, 3021

White, M., Raichoor, A., Dey, A., et al. 2024, JCAP, 2024, 020

Xu, C., Smith, A., Borrow, J., et al. 2023, MNRAS, 521, 4356

Zarattini, S., & Aguerri, J. A. L. 2025, arXiv e-prints, arXiv:2504.02026